Microstructural evolution and resulting properties of differently sintered and heat-treated binder jet 3D printed Stellite 6

Amir Mostafaei [a,*,1], Pierangeli Rodriguez De Vecchis [a], Michael J. Buckenmeyer [b], Sumant R. Wasule [c], Bryan N. Brown [b,d], Markus Chmielus [a,*]

[a] Department of Mechanical Engineering and Materials Science, University of Pittsburgh, Pittsburgh, PA 15261, USA

[b] Department of Bioengineering, McGowan Institute for Regenerative Medicine, University of Pittsburgh, Pittsburgh, PA 15219, USA

[c] Department of Metallurgical Engineering and Materials Science, Indian Institute of Technology, Bombay, Mumbai 400076, India

[d] Department of Obstetrics, Gynecology and Reproductive Sciences, Magee-Womens Hospital, Pittsburgh, PA 15213, USA

[1] Current address: Department of Materials Science and Engineering, Carnegie Mellon University, Pittsburgh, PA, 15213, USA

* Corresponding authors

Email addresses: amir.mostafaei@pitt.edu (A. Mostafaei); chmielus@pitt.edu (M. Chmielus)

Abstract

Stellite 6 components are manufactured from gas-atomized powder using binder jet 3D printing (BJ3DP) followed by curing and sintering steps for densification. Green parts are sintered at temperatures ranging from 1260 °C to 1310 °C for 1 h. Microstructural evolution and phase formation during sintering and aging are studied by optical and scanning electron microscopy, elemental analysis and X-ray diffraction. It was found that solid-state sintering was present at temperatures below 1280 °C with Cr-rich carbides present within grains; while supersolidus liquid phase sintering was the dominant sintering mechanism during sintering at 1290 °C and higher in which the Co-rich solid solution regions are surrounded by eutectic carbides. Sintering at 1300 °C resulted in the maximum density of ~99.8%, mean grain size of ~98 ± 6 μm with an average hardness of 307 ± 15 $HV_{0.1}$ and 484 ± 30 $HV_{0.1}$ within grain and at the boundaries, respectively. Aging was performed at 900 °C for 10 h leading to the martensitic transformation (fcc→hcp) as well as an increase in eutectic carbides at boundaries and nano-sized carbides within grains where the average hardness within grains and boundaries was enhanced to 322 ± 29 $HV_{0.1}$ and 491 ± 58

$HV_{0.1}$, respectively. Fibroblasts seeded on top of 3D-printed Stellite 6 discs displayed a cell viability of 98.8% ± 0.2% after 48 h, which confirmed that these materials are non-cytotoxic. Presented results demonstrate that binder jetting can produce mechanically sound complex-shaped structures as shown here on a denture metal framework and small-scale knee model.

Keywords: Co-Cr-W alloy; Additive manufacturing; Sintering; Porosity; Cytocompatibility.

1. Introduction

Co-Cr-based (Stellite) alloys have been extensively used in aerospace, marine, automotive, petrochemical, and medical applications due to their excellent properties such as high strength, wear/corrosion resistance and hardness [1–4]. Applications as well as properties of Stellite alloys are widely determined by their chemical compositions [5]. Alloying elements such as Cr, W, and Mo contribute to strengthen Co-Cr-based alloys with the formation of a solid solution matrix; however, carbide precipitates are the other strengthening segments [6,7]. Stellite 6 with a nominal composition of Co–28Cr–4.5W–1.2C (wt.-%) was the first Stellite alloy developed in the early 1900s by Elwood Haynes [1]. Traditional processing methods for part production of Stellite alloys include casting, forging, milling and hot isostatic pressing [8–13]. Due to presence of tungsten, it is intrinsically difficult and expensive to machine this alloy. Complex-shaped components can be manufactured by means of powder injection molding (PIM) [4]; however, it is not feasible to produce parts with internal and external porosity/microchannel.

As an alternative, additive manufacturing (AM) has attracted attention to produce complex parts from different materials. Mengucci et al. [14] studied direct metal laser sintering (DMLS) of Co-Cr-Mo-W alloys followed by a post treatment that resulted in an intricate network of ε-Co (hexagonal close-packed (hcp) structure) lamellae in the γ-Co (face-centered cubic (fcc) structure) matrix with a high hardness value. It was shown that the thermal treatments are capable of increasing volume fraction of the ε-Co (hcp) martensite as well as producing massive precipitation

of an hcp $Co_3(Mo,W)_2Si$ phase and the formation of Si-rich inclusions. However, the applied heat-treatment was intended for porcelain fused metal crowns; hence, the fabricated part was subjected to a complex firing procedure specifically for veneering with a dental ceramic material. Ren et al. [15] showed that as-deposited Co-Cr-W samples fabricated by laser AM had few cracks or pores with a typical dendritic structure, and lamellar eutectic carbides microstructure. Additionally, some γ-phase transformed into ε-phases after an aging treatment (at 900 °C/6 h) and lamellar eutectic carbides transformed into a network of blocky carbides. Most of the carbides were rich in Cr and a few sub-micron-sized precipitates were rich in W forming at the grain boundaries.

One drawback of fusion based AM techniques is the large amount of residual stress in the fabricated part leading to crack formation [15–18]. Binder jet 3D printing (BJ3DP), a non-beam based AM method, refers to the technology in which powdered material is deposited layer-by-layer and which are selectively joined with binder and then densified through sintering [19–23]. Binder jetting of metals holds distinctive promise among AM technologies due to its fast, low-cost manufacturing; stress-free, mechanically sound structures with complex internal and external geometries as shown in this study on a complex-shaped denture framework with fine details and small-scale knee model; and the isotropic properties of the final parts [24,25]. Also, by taking advantage of traditional powder metallurgy, binder jet 3D printers can produce prototypes for biomedical applications from [26–32] metal parts in which material properties and surface finish are similar to those achieved with PIM or traditional powder metallurgy [33].

In this work, the microstructures and hardness of Stellite 6 (or Co–Cr–W alloy) specimens produced by BJ3DP followed by sintering and post heat-treatment were examined. A detailed analysis on the densification, porosity and phase formation were carried out to understand how microstructural evolution occurred based on the sintering and post treatment steps.

2. Materials and methods

In this study, gas atomized Stellite 6 powder was supplied by Kennametal Inc. (Irwin, PA, USA). The particle size distribution by volume percentile was analyzed using a Microtrac S3500 tri-laser diffraction particle analysis system via algorithms for spherical particles. A powder particle sample of approximately 1 g was suspended in isopropyl alcohol which also possibly prevented agglomeration. The particle size distribution result is shown in Figure 1a and the obtained values are: d_{10} = 90.4 μm, d_{50} = 94.2 μm and d_{90} = 110.1 μm. Morphology - exemplary size distribution, and the dendritic structure - of the rapid solidified gas-atomized Stellite 6 powders are illustrated in Figure 1b. Most powder particles were spherical in shape having a mean particle size of ~95 μm with small satellites on surface. An inset SEM micrograph (see Figure 1b) indicated a dendritic structure on powder particles which was typical of rapid solidification during the atomization process [34]. Chemical composition of the feedstock powder is given in Table1. Carbon, oxygen and nitrogen content were measured using LECO (models ONH836 and CS844).

To produce 3D printed parts, an X1-Lab binder jet 3D printer (ExOne, North Huntington, PA) was used to manufacture coupons from Stellite 6 powder with dimensions of 7×7×7 mm^3. BJ3DP parts were produced with an ethylene glycol monomethyl ether and diethylene glycol solvent binder with a layer thickness of 200 μm, spread speed of 20 mm/s, feed/built powder ratio of 2, drying time of 40 s and binder saturation of 40%. Besides, an Innovent binder jet 3D printer (ExOne, North Huntington, PA) was used to produce small scale-knee and partial denture framework with the printing parameters of: layer height of 100 μm, recoat speed of 90 mm/s, oscillator speed of 2100 rpm, roller speed of 350 rpm, roller traverse speed of 15 mm/s, and drying time of 20 s. Printed parts were cured at 200 °C in a Carbolite oven for 8 h and then sintered in a Lindberg tube furnace under vacuum (the vacuum level was ~10^{-5} bar) with the following heating

profile: heating at 5 °C/min from room temperature to holding temperature ranging from 1260 to1310 °C in intervals of 10 °C with a holding time of 1 h and then cooling at 5 °C/min to 800 °C and finally furnace cooling to room temperature. The measured solidus and liquidus temperatures for the used alloys were reported by Kennametal Co. to be 1265 °C and 1361 °C, respectively, in agreement with [35]. Thus, the selected sintering temperatures led to solid state or liquid phase sintering. Four samples for each sintering temperature were prepared. An aging treatment at 900 °C for 10 h was conducted on selected samples with the highest relative density.

Relative density of the sintered samples was measured via the submersion Archimedes method (three samples were immersed in deionized water) with an OHAUS AX324 precision balance (0.1 mg resolution) as well as from cross-sectional micrographs with the ImageJ image analysis software [36] after taking images using a Keyence digital optical microscope (three samples at magnifications of ×200). For microstructural examination of the sintered coupons, cross sections were cut from the specimens, mounted, ground and polished using a Struers Tegramin-25 automatic system according to [37]. Then, micrographs were taken with a Zeiss Smartzoom 5 Digital Microscope. Grain and pore size measurements were carried out according to [38]. Microstructural observation and elemental composition analysis of the powder as well as the sintered and heat-treated parts were conducted with a ZEISS Sigma 500 VP scanning electron microscope (SEM) equipped with energy dispersive x-ray spectroscopy (EDS). Phase identification and crystallography parameters such as *d*-spacing values and lattice parameters were determined using an x-ray diffractometer (XRD, Bruker AXS D8 Discover) with Cu–Kα radiation (λ = 1.54 Å, 40 kV, 40 mA) with a step of 0.02°, a scan speed of 0.5 s/step and 2θ ranging from 35° to 95° at room temperature. Vickers microhardness tests were performed on the cross sections of samples with a Leco LM 800 microhardness tester (100 gf for 10 s). Twenty indentations were

performed at the grains and boundaries and average values were reported. Rate controlled tensile test at 5 mm/min was performed on the samples sintered at 1300 °C for 1 h and an additional sample aged at 900 °C for 10 h using a MTS 880. For the mechanical testing, an ASTM standard test method for tension testing of metallic materials (ASTM Standards E8) was used.

To test the materials' *in vitro* cytotoxicity, NIH/3T3 fibroblasts (ATCC® CRL-1658™) were seeded on top of 3D printed Stellite 6 (samples sintered at 1300 °C with the root-mean-square roughness, also called R_q, of 3.7 ± 0.2 μm using a stylus profilometer (Alpha-Step IQ, KLA-Tencor, Milpitas, California, USA)) discs for 48 h and stained with fluorescent markers to evaluate cell viability. Fibroblasts were cultured as recommended by ATCC®. Briefly, cells were plated at a density of 3-5x10^3 cells/cm^2 in cell culture treated flasks and cultured in complete growth medium (Dulbecco's Modified Eagle's Medium (DMEM), 10% Bovine Calf Serum (BCS), and 1% Penicillin/Streptomycin). Stellite 6 discs (five disks were tested) were made to fit the diameter of a 12-well plate (BioLite) and autoclaved to ensure sterility. Discs were soaked in complete growth medium for a minimum of 2 h prior to the addition of cells. Fibroblasts were seeded at a density of 1.0x10^5 cells/well and incubated at 37°C (95% air, 5% CO_2) for two days. To evaluate the cytotoxicity of binder-jet 3D printed and sintered Stellite 6, a LIVE/DEAD™ Viability/Cytotoxicity Kit (Invitrogen™ - L3224) was used according to manufacturer's instructions. Cell culture treated polystyrene (CCTP) was used as a positive control (+Control). Ethanol-killed cells on CCTP was used as a negative control (-Control) and was prepared by treating cells with 70% ethanol for 30 min. Briefly, complete growth medium was removed from each well, then cells were washed with Hank's Balanced Salt Solution (HBSS) (Gibco®) to remove any interfering serum proteins from the discs. A warmed solution of 2 μM Calcein AM and 4 μM Ethidium homodimer-1 prepared in HBSS was added to each well. The plate was then incubated

for 30 min at 37 °C (95% air, 5% CO_2). Live/Dead solution was removed and replaced with fresh complete growth medium. Five images were taken of each sample well using an inverted light microscope (Nikon Eclipse Ti-U). Images (n = 15/group) were analyzed using CellProfiler (Version 3.0) to quantify the total number of live and dead cells.

3. Results and Discussion

3.1. Density and microstructure studies

Relative bulk density of the green part was found to be ~48 ± 1%. For the sintered parts, the relative bulk density results (Archimedes method) as well as the solid volume fraction measurements (optical image analysis on cross sections) are shown in Figure 2. Results show that the density increased with increasing temperature. Sintering at 1260 °C and 1270 °C resulted in porous samples with an average density of ~55% and ~57%. By increasing the sintering temperature to 1280 °C, the relative density increased up to ~70% and reached a significantly higher ~95% at 1290 °C. The highest relative density was achieved ~99.8% at sintering temperatures of 1300 °C. Finally, increasing sintering temperature to 1310 °C resulted in surface melting and shape change of the printed sample and the relative bulk density slightly decreased to 99.1%. Gülsoy et al. [12] produced parts from gas atomized Stellite 6 with average particle size of ~14 μm using PIM method with the maximum relative density of ~98.3% at 1275 °C. Other researchers applied hot isostatic pressing (HIP) method to reach full density [9,39].

Figure 3 illustrated cross-sectional optical micrographs of shape, size and distribution of grains, porosity and precipitates as well as microstructural evolution of the BJ3DP samples made from Stellite 6 powder sintered ranging from 1260 °C to 1310 °C for 1 h and Table 2 summarizes the quantitative results for all sintering temperatures. In general, a progression with increasing sintering temperature from irregular, interconnected pores to disconnected spherical pores within

the grains or located at the grain boundaries was observed. This was accompanied by pore size shrinkage. Sintering at 1260 °C (solid volume fraction ~56%) resulted in neck formation between neighboring particles (see Figure 3a) and pores located in intergranular regions. Additionally, small precipitates were formed within grains. Image analysis results are summarized in Table 2 and show nearly similar grain. Since Stellite 6 is a Co-based superalloy, it is expected that the matrix is Co-rich with Cr-rich precipitates. OM analysis of the sample sintered at 1260 °C showed that ~45% of OM micrograph consisted of Co-rich grains while ~12% was made of Cr-rich carbides within grains. As the temperature increased to 1270 °C (Figure 3b), sinter necks expanded and the solid volume fraction increased to ~58% with a grain size of ~70 μm. Moreover, it was found that the amount of Cr-rich carbides within grains increased slightly up to ~14%. A more substantial microstructural change in terms of grain size and pore size started for the sample sintered at 1280 °C (Figure 3c) where the solid volume fraction increased to ~71% with average grain size of ~89 μm. Besides, the pore network seemed to be broken down to smaller, closed volumes. Furthermore, two types of Cr-rich precipitates were observed in micrographs of the sintered sample at 1280 °C: as before, small-size precipitates within grains (~10% of the micrographs) and new Cr-rich precipitates at grain boundaries (~6% of the micrograph). As the sintering temperature increased to 1290 °C and above, significant changes in microstructure, densification, grain and pore sizes were observed as shown in Figure 3d-f. For the sample sintered at 1290 °C, the OM showed a solid volume fraction of ~97.5%, average grain and pore size of ~100 μm and ~8 μm, respectively. Interestingly, no precipitates were detected within grains while eutectic carbides probably enriched in chromium were observed at the grain boundaries (~16% of the OM micrographs shown in Figure 3d). Sintering at 1300 °C significantly decreased the porosity level and the solid volume fraction reached ~99.8% eliminating the majority of pores (average

size: ~5 μm) from the grains and boundaries. The small spherical pores instead of irregularly shaped pores is a desired condition in terms of strength. It was seen that the grain size decreased slightly and within the standard deviation from ~100 μm to ~94 μm as the sintering temperature increased from 1290 °C to 1310 °C. Furthermore, the Co-rich area fraction decreased from ~84% to ~78% while the Cr-rich eutectic carbides (formed at the grain boundaries area) fraction increased from ~16% to ~22%. It is known that the grain size during sintering increases with sintering temperature and duration [40], which is also shown here when increasing sintering temperature from 1260 °C to 1290 °C; while the sample sintered at 1310 °C showed no grain growth or even slight reduction in the average grain size. It was thought that the eutectic carbides precipitating at the surroundings of the Co-rich matrix at the grain boundaries played an inhibitive role in further grain coarsening.

Finally, the slight differences between density measured via Archimedes vs solid volume fraction extracted from 2D micrographs could be indicative of regions evaluated via OM with slightly less pores or pores small enough to be missed in the 2D optical micrographs.

3.2. Electron microscopy and elemental analysis

Carbon (C), oxygen (O) and nitrogen (N) are of high importance with regards to phase formation, mechanical properties and cytocompatibility (see Table 3 for wt.-% of these elements in all samples). It was seen that the C, O and N content of the as-received Stellite 6 powder was 1.238 wt.-%, 0.058 wt.-% and 0.025 wt.-%, respectively, which increased to 1.570 wt.-%, 0.114 wt.-% and 0.142 wt.-% after binder jetting followed by the curing step due to the C, O and N content in the binder. Interestingly, C content is below the original powder content for every sintering step; for N and O this is also the case for the highest sintering temperatures. The increase of the three elements after printing and curing is from the binder in the samples at this stage of

post-processing, while the reduction during sintering is caused by binder burn-out and potentially due to decomposition/desorption of C, N and O rich layers existing on the surface of the original particles.

Figure 4 showed SEM micrographs with EDS mapping elemental analysis results at different temperatures sintered Stellite 6 BJ3DP samples. In general, Stellite 6 cast alloy has a microstructure consisting of Co-rich matrix as the solid solution region with a light gray color and an interdendritic eutectic comprising of Cr-rich M_7C_3 and/or $M_{23}C_6$ carbides [1–3,9,39]. Depending on the sintering temperature, different microstructures in terms of precipitate formation were seen in the here produced BJ3DP samples. Sintering at 1260 °C (Figure 4a, porous final microstructure) resulted in uniformly distributed fine carbides (dark phase) in a Co-rich matrix (light grey region) with sizes ranging from sub-micron to 5 μm. This microstructure was similar to the microstructure of hot isostatic pressed (HIPed) parts where nearly spheroidal carbides enriched in C, Cr and Mn and poor in Co are uniformly distributed in Co-rich solid solution regions [1,7]. As the sintering temperature increased to 1280 °C, the microstructure evolved further (see Figure 4b): densification and necking growth occurred. Shape and size of the formed precipitates slightly changed as well to fine granular precipitates mainly dispersed in the center of grains and continuous precipitates formed at grain boundaries. EDS mapping indicated that, both, precipitates within the grains and at the grain boundaries consisted of Cr, Mn and C. A zone around the grain boundaries within in the grains showed no precipitates most likely due to depletion of precipitation forming elements. Cr and C are solid solution elements within the used Stellite 6 gas atomized powder. During sintering, Cr-rich carbides might form depending on the sintering temperature. At temperatures below 1270 °C, $Cr_{23}C_6$ may form within grains. At temperatures above 1270 °C, carbon might diffuse from the matrix to the grain boundaries and a eutectic phase may form in Co-

Cr-C ternary composition. The eutectic carbides (mostly Cr_7C_3 with little trace of $Cr_{23}C_6$) formed at grain boundaries might be due to liquid phase formation above 1270 °C. As the sintering temperature increased up to 1310 °C, the fraction of liquid phase increased as well leading to a higher content of eutectic carbides at the grain boundaries. The formation of $Cr_{23}C_6$ was most likely due to the controlled cooling at a rate of 5 °C/min at sintering temperatures below 1270 °C. Similar results were reported in [3,12].

The microstructure of casted Stellite 6 consists of dendrites formed by Co solid-solution and eutectic carbide phases, and dendrites between them due to slow solidification during casting. In a study by Liu et al. [35], it was shown for a Co-28Cr-4W-1.3C alloy that the primary Co matrix with a interdendritic Cr-enriched phase could form. A similar hypoeutectic microstructure (lamellar morphology) was seen here when sintered at 1290 °C and higher (see Figure 4c, sintered at 1300 °C) which consisted of the Co-rich matrix (light gray) and the continuous Cr-rich carbides (dark gray) at the grain boundaries. No fine granular precipitates were seen indicating that all primary precipitates converted to secondary precipitates at the boundaries. The lamella structures were most likely formed during cooling at temperatures under 990 °C [8].

Typically, Co-based superalloys gain their strength from the solid solution hardening and the carbide precipitates [41]. Cr is the most significant alloying element for Co-based superalloys since it is not only a predominant carbide former but also contributes to the solid solution hardening [11,12,42]. Cr and Mn in Co-based superalloys can form MC, M_3C_2, M_7C_3, and $M_{23}C_6$ carbides. M_3C_2 and MC carbides may form with a high C content. Typically, M_7C_3 carbides form more in intragranular regions and sometimes intergranular regions. Importantly, M_7C_3 carbides are metastable and partially transform into the $M_{23}C_6$ carbides during heat-treatments or under high temperature service conditions [6,43]. The used Stellite 6 powder has a considerably high Cr-

content of 30.2 wt.-%, and about <1 wt.-% C. Thus, $M_7C_3/M_{23}C_6$ carbides can precipitate as both primary and secondary carbides due to the high Cr-content. The precipitates formed in the printed and sintered samples are thought to be $M_{23}C_6$ carbides within the grains and mixed $M_7C_3/M_{23}C_6$ carbides at the grain boundaries.

3.3. Influence of Aging on Microstructure

The effect of aging on the microstructural evolution was studied on the samples sintered at 1300 °C which showed maximum density of 99.8%. OM micrographs of BJ3DP samples sintered at 1300 °C (Figure 5a-b) show Co-rich grains with an average grain size of ~98 μm surrounded by eutectic carbides (see Table 2), a solid volume fraction of ~99.8%, the Co-rich fraction of ~83% and eutectic carbides fraction of ~16.8% at the grain boundaries. After aging at 900 °C for 10 h, the average grain size stayed nearly constant with ~94 μm, the Co-rich fraction decreased to ~72% and the eutectic carbides fraction at the grain boundaries significantly increased to ~27.8%. Additionally, some eutectic carbides formed in grains with pores which might have helped to slightly increase the relative bulk density.

SEM micrographs of the sintered and aged BJ3DP samples (Figure 6) show, similarly to the OM micrographs, that the BJ3DP Stellite 6 samples sintered at 1300 °C consist of Co-rich matrix surrounded by Cr-rich carbides. After aging (900 °C for 10 h), Co-based superalloys typically experience a martensitic transformation (as indicated by intragranular striations in Fig. 6 c and d) in which the γ-phase (Co-rich matrix) transforms to the ε-phase [17,44,45]. Besides, bright white sub-micron precipitates formed at the grain boundaries and within grains. The fine isothermal ε martensite plates formed during the early stage of the heat-treatment. As the heat-treatment progressed, some precipitates may form in the microstructure in agreement with [7].

EDS maps of the aged samples (Figure 7) indicate that three types of precipitates were present after aging at 900 °C for 10 h: (1) Cr-rich carbides at grain boundaries that were formed during sintering at 1300 °C and increased in size during aging, (2) nano-sized $M_{23}C_6$ carbides formed in the Co-rich matrix during aging (as also was reported in [46]), and (3) W-rich $M_{23}C_6$ carbides (light colored precipitates at grain boundaries) that contained other alloying elements such as Si, W and Mo forming MSi_2 (M = Mo and W). It was thought that the W-rich carbides might contain silicide as a distinct, very fine sub-phase [35,47]. Ren et al. [15] fabricated Co-Cr-W parts by laser additive manufacturing and reported the formation of similar precipitates after aging (900 °C for 6 h). In Co-based superalloys, W and Mo elements are added to enhance hardening via solid solution of the matrix due to their large atom sizes. As the amount of W and Co are high in Stellite 6, the chance of carbides or intermetallic compounds formation is increased [7,15].

3.4. Phase analysis using X-ray diffraction

Figure 8 illustrated X-ray diffraction patterns of differently sintered (and aged) BJ3DP Stellite 6 samples. Only peaks of γ-Co with fcc crystal structure were seen in the XRD pattern of the Stellite 6 powder with the calculated *d*-spacing value of 2.07 Å at the peak position of 43.80°. After sintering at 1260 °C, the diffraction peaks shifted slightly to higher angles. By increasing the sintering temperature from 1260 °C to 1300 °C, the peaks shifted from 43.86° to 44.08° and, thus, the *d*-spacing decreased slightly to 2.06 Å. This reduction in matrix *d*-spacing values can be attributed to elemental depletion due to precipitate formation within grains or at the grain boundaries. As the sintering temperature increased to 1310 °C, further peak shift was seen and the *d*-spacing decreased to 2.04 Å. In Figure 3 it was seen that more eutectic carbides were formed in the sample sintered at 1310 °C compared to the one sintered at 1300 °C. XRD also showed that hcp ε-Co formed after sintering at 1310 °C. Few additional diffraction peaks were seen in samples

sintered at 1280 °C and higher indicating carbide formation during sintering. XRD pattern of the sample sintered at 1300 °C followed by aging treatment indicated that the matrix was mainly composed of hcp ε-Co. $M_{23}C_6/M_7C_3$ carbides peaks were also found in the diffraction pattern of the aged sample. It was reported that some but not all peaks of the $M_{23}C_6$ carbide coincide with the peaks of the Co matrix [12,47]. The peaks of $M_{23}C_6/M_7C_3$ carbides in the sintered material at 1280 °C and higher became more apparent. Due to sintering at high vacuum and in the presence of Ti sponge, oxidation was prevented and, therefore, no oxide diffraction peaks were identified. The amount of Cr in the used Stellite 6 powder was about 30%, similar to Gülsoy et al. [12] who showed that $M_{23}C_6$-type carbides can precipitate as both the primary and secondary carbides in high Cr content. Yingfei et al. [3] and Kilner et al. [48] reported that "pearlitic" colonies may form during continuous cooling at around 990 °C at grain boundaries and consisted of interlayed plates of $M_7C_3/M_{23}C_6$ and fcc Co-rich γ-phase. Aging at 900 °C can increase these pearlitic colonies at the grain boundary [8,49] which was observed in our study.

3.5. Mechanical properties

The microhardness measurements (Figure 9a) of the differently sintered and aged BJ3DP Stellite 6 samples show a general trend of increasing hardness with sintering temperature most likely due to the increasing density of the samples. Two different hardness values were measured: within grains and at the grain boundaries. The average hardness within grains (due to low density of ~57% and, thus, limited grain boundaries) increased slightly from ~220 $HV_{0.1}$ (sintered at 1260 °C) to ~284 $HV_{0.1}$ (sintered at 1270 °C with slightly higher density). This was expected due to their very similar microstructure (see Figure 3). However, the microstructure of the sample sintered at 1280 °C showed first changes with increased necking and densification (~71% density), and the formation of eutectic and secondary pearlitic carbides formation at grain boundaries. The density

increase and carbide formation resulted in an average hardness of 286 $HV_{0.1}$ and 370 $HV_{0.1}$ at the grains and grain boundaries, respectively. Higher sintering temperature resulted in further densification while phase formation within grains and at the boundaries evolved further. Increasing sintering temperature to 1310 °C led to the removal of carbides from the grains however, the pearlitic carbide increased at the grain boundaries. Hardness measurements showed hardness values between 318 $HV_{0.1}$ and 453 $HV_{0.1}$ within grains and grain boundaries, respectively, for samples sintered at 1290 °C. Increasing the sintering temperature to 1310 °C resulted in hardness reduction within grain (~300 $HV_{0.1}$) and enhancement at the boundaries (~491 $HV_{0.1}$). This might be associated with the Cr and Mn depletion from grains and formation of $M_7C_3/M_{23}C_6$ carbides at the boundaries. Aging of the sample sintered at 1300 °C increased the average hardness values within grain from 307 $HV_{0.1}$ to 322 $HV_{0.1}$, and at the grain boundaries from 484 $HV_{0.1}$ to 492 $HV_{0.1}$. This hardness increment can be attributed to the phase transformation from fcc to hcp in the Co-matrix, the nano-scale carbides within grains, and formation of more pearlite and W-rich carbide/silicide at the grain boundaries. It was reported that the hardness of casted and conventional powder metallurgy Stellite 6 samples is ~400 HV [50]. Gülsoy et al. [12] reported a hardness of 460 $HV_{0.5}$ for PIM small-sized pre-alloyed Stellite 6 powder samples sintered at 1275 °C (relative density ~ 98.3%) which is higher than the here reported hardness. The improved hardness compared to our study might be due to the used fine powder, grain structure and grain size of the materials produced by using PIM as well as morphology and distributions of carbides.

Tensile test stress-strain curves of fully densified sintered and aged samples (Figure 9b) showed a UTS, yield stress and elongation of ~853 MPa, ~575 MPa and ~10.5%, respectively, for the sintered samples and ~885 MPa (UTS), ~581 MPa (yield stress) and ~1.7% (elongation) for the sintered and aged samples. The UTS and elongation of the cast Stellite 6 are reported as 911

MPa and ~1% (Kennametal), very similar to the sintered and aged BJ3DP samples, while the sintered-only samples show 10-fold larger elongation with 8% lower UTS. It was thought that the formation of higher eutectic carbide at the grain boundary and formation of martensite in Co-rich grains led to the reduction of ductility. SEM micrographs of the fracture surfaces illustrated as and inset in Figure 9b indicate mostly brittle fracture for both sintered and aged samples. In the aged sample, some pull-off grains were seen due to the higher content of pearlitic colonies formed at the boundaries. The crack propagation around the grains and across the intergranular pearlitic colonies is similar to fracture surfaces observed for the cast and injection molded Co-Cr-W alloy in [3,12]

3.6. Microstructural evolution during sintering of BJ3DP Stellite 6

The sintering process is an important microstructure and property-defining step in BJ3DP of metal powder leading to densification of the green part due to diffusion at high temperature. The green part strength is achieved during the curing step by crosslinking of the polymeric binder, while desired mechanical properties can be attained after sintering and potentially additional aging with a controlled large variation of final densities and microstructures. Figure 10 illustrates the microstructural evolution at different steps during sintering and aging of Stellite 6. In BJ3DP parts, the green parts density is usually 40-50% and the driving force of sintering is primarily based on the reduction of surface energy.

In the as-printed and cured BJ3DP Stellite 6 samples, green part density was ~49%. At this stage, bonding between powder particles is solely due to the cured binder. Controlled by the temperature during sintering, different mechanisms including solid-state sintering or supersolidus liquid phase sintering are present. For the used Stellite 6 powder, a ***low temperature sintering regime*** exists at temperatures below 1280 °C with surface diffusion at contact points of adjacent

particles usually as the dominant mass-transport mechanism during the early stages of neck formation [51,52]. Thus, there is no significant dimensional change or porosity reduction in initial stage or low temperature sintering. In this regime, primary carbides are formed within grains as OM and SEM micrographs showed in Figure 3 and Figure 4, respectively. Stellite 6 powder is a pre-alloyed compound produced by gas atomization method with alloying elements such as Cr, W, Mo and C. Mo and W have large atomic radii and, thus, have considerably low diffusion coefficients to find sufficient time to form carbides during the gas atomization step. Consequently, Cr has a higher chance to form carbides in Co-based superalloys such as M_6C, M_3C_2, M_7C_3 and $M_{23}C_6$ carbides (M = Co, Cr, W, Fe, Ni, Si). Generally, the M_6C-type carbides are Mo-rich and the other carbides are Cr-rich carbides. In the used Stellite 6 alloy, there was 0.7 wt.-% Mo, thus, M_6C carbide was not expected to form and $M_{23}C_6$ the most likely to form in the low temperature sintering regime.

The ***medium temperature sintering regime*** takes place at temperatures from 1280 °C up to 1290 °C with grain boundary and volume diffusion being dominant. Therefore, parts experience a significant amount of densification to up to ~95% (see Figure 10, intermediate stage). At this stage, pore channels start to close and create isolated porosity via neck growth and the creation of new contact points during pore shrinkage. Material migrates from inside the particles to the surface, resulting in contact flattening and densification. Since the temperature is high enough, the formed primary carbides within grains can migrate to the grain boundaries and form secondary carbides.

The ***high temperature sintering regime*** occurs at temperatures higher than 1300 °C to 1310 °C. In this final sintering regime, the maximum density is achieved by elimination of closed pores. Since the solidus and liquidus temperatures of Stellite 6 are reported to be 1270 °C and

1360 °C, respectively, it is thought that partial melting was formed which resulted in the pearlitic colony formation made of carbides and Co. Further heat-treatment. i.e. aging at 900 °C for 10 h, resulted in the isothermal $\gamma \rightarrow \varepsilon$ martensitic transformation and the increase of the volume fraction of the pearlitic colonies. As seen in the SEM micrographs of the aged samples (Figure 7), two new precipitates formed during the aging process including (1) W-rich carbide (red spots in Figure 10) in form of M_6C/ $M_{23}C_6$ contained other alloying elements such as Si and Mo and (2) nano-sized $M_{23}C_6$ carbides. Microstructural results were in agreement with Liao et al. [53] and Yamanaka et al. [54] observations. The phase transformation of γ-fcc $\rightarrow$ ε-hcp and the carbide formations were in good agreement with the results of the thermodynamic calculations illustrated in Figure 11.

3.7. Biomedical application and cytotoxicity study of BJ3DP Stellite 6

Figure 12 illustrated examples of Stellite 6 BJ3DP parts showing the capabilities of BJ3DP of complex parts for biomedical applications on the example of a thin-walled partial denture frame and a small-scale knee joint, all sintered at 1280 °C for 1 h to consolidate parts. It is apparent that parts with internal and external complexity can be produced using BJ3DP followed by sintering step. During the sintering step, it is important to control densification rate and shrinkage in the BJ3DP part in order to assure parts can retain the original printed shape. Based on our experience, sintering in an alumina powder bed can provide uniform heat conduction during sintering as well as prevention of sagging and deformation of overhanging structures. Depending on the required porosity and mechanical strength, various sintering and aging treatments can be designed to achieve desired microstructure and properties.

Merged FITC and TRITC fluorescent images (Figure 13A) indicate that fibroblasts successfully adhered to the Stellite 6 discs, with the majority of cells displaying a FITC signal, representative of healthy cells. The spindle-like projections exhibited by the cells signify normal

fibroblast morphology and suggest that cell motility is not impaired. When comparing the Stellite 6 group to the +Control, no discernible differences in cell viability were observed; however, there did appear to be a decrease in the cell density for Stellite 6 in relation to the control groups. The disparity in the number of cells on the Stellite 6 discs could be attributed to the differences in material composition. CCTP is known to have modified surfaces that improve cellular attachments, whereas on materials such as Stellite 6, de novo synthesis and adsorption of matrix proteins must occur for focal adhesion. The area of the Stellite 6 discs was also slightly smaller than each well, which could have resulted in a decrease of total cells exposed to the Stellite 6 surface. A semi-quantitative image analysis was performed to measure the percentage of viable cells and the total number of Live/Dead cells in each treatment group. Cells cultured on top of Stellite 6 discs displayed a 98.82% ± 0.23% (mean ± SEM) viability, which did not vary significantly from the +Control (99.37% ± 0.18%) (Figure 13B). A significant decrease in the total number of Live cells in comparison to the +Control was confirmed in the Stellite 6 group after quantification (Figure 13C); however, the relative number of Live/Dead cells and cell viability indicate that the Stellite 6 material is non-cytotoxic.

4. Conclusion

This study has investigated the microstructural evolution, mechanical behavior and cytotoxicity properties of the binder jetted parts from gas atomized Stellite 6 powder during sintering. Based on the results, the following conclusions are drawn:

1. As-printed parts had a green density of ~48% and after sintering between 1260 °C and 1310 °C for 1 h, relative density of 55% and 99.8% were attained, respectively.

2. Microscopy observations showed that the grain diameter of the sample sintered at 1260 °C was between 64 ± 2 μm, while it increased to 98 ± 6 μm after sintering at 1300 °C. Additionally,

an evolution in carbide formation was seen such that in grain carbide precipitates formed at sintering temperatures <1290 °C where solid-state sintering was the active sintering mechanism; while at temperatures of ≥1290 °C, supersolidus liquid phase sintering was present and the pearlitic carbide colonies formed at the boundaries where an average hardness of 307 ± 15 $HV_{0.1}$ and 484 ± 30 $HV_{0.1}$ within grain and at the boundaries, respectively.

3. Phase analysis and microscopy observations showed that aging treatment at 900 °C for 10 h resulted in the martensitic transformation (γ-fcc → ε-hcp) as well as an increase in eutectic carbides at boundaries and nano-sized carbides within grains where the average hardness within grains and boundaries was enhanced to 322 ± 29 $HV_{0.1}$ and 491 ± 58 $HV_{0.1}$, respectively.

4. Fibroblasts cultured on top of Stellite 6 discs exhibited normal cell morphology and attachment to the material surface after 48 h. Quantitative image analysis of Live/Dead cells showed no significant difference in cell viability between the Stellite 6 group and CCTP (+Control) providing evidence that Stellite 6 supports cell survival.

5. This study showed that binder jetting was capable of manufacturing complex geometries with fine features such as a partial denture framework and small-scale knee joint.

Acknowledgements

P.R.D.V. would like to acknowledge partial funding through the NSF CMMI 1727676 REU supplement. The authors would like to thank Paul Prichard and Kennametal Inc. for providing Stellite 6 powder as well as C, O and N elemental analysis. The authors would like to thank Runbo Jiang for assisting with Thermodynamic modeling. This work was performed, in part, at the Nanoscale Fabrication and Characterization Facility, a laboratory of the Gertrude E. and John M. Petersen Institute of NanoScience and Engineering and the ANSYS Additive Manufacturing Research Laboratory, housed at the University of Pittsburgh.

References

[1] F. Rosalbino, G. Scavino, Corrosion behaviour assessment of cast and HIPed Stellite 6 alloy in a chloride-containing environment, Electrochim. Acta. 111 (2013) 656–662.

[2] V. V Kuznetsov, E.A. Filatova, A. V Telezhkina, S.S. Kruglikov, Corrosion resistance of Co − Cr − W coatings obtained by electrodeposition, (2018) 2267–2276.

[3] G. Yingfei, P.M. de Escalona, A. Galloway, Influence of Cutting Parameters and Tool Wear on the Surface Integrity of Cobalt-Based Stellite 6 Alloy When Machined Under a Dry Cutting Environment, J. Mater. Eng. Perform. 26 (2017) 312–326.

[4] Ö. Özgün, İ. Dinler, Production and Characterization of WC-Reinforced Co-Based Superalloy Matrix Composites, Metall. Mater. Trans. A. 49 (2018) 1–13.

[5] J.C. Shin, J.M. Doh, J.K. Yoon, D.Y. Lee, J.S. Kim, Effect of molybdenum on the microstructure and wear resistance of cobalt-base Stellite hardfacing alloys, Surf. Coatings Technol. 166 (2003) 117–126.

[6] A. Khoddamzadeh, R. Liu, M. Liang, Q. Yang, Novel wear-resistant materials - Carbon fiber reinforced low-carbon Stellite alloy composites, Compos. Part A Appl. Sci. Manuf. 43 (2012) 344–352.

[7] R. Ahmed, A. Ashraf, M. Elameen, N.H. Faisal, A.M. El-Sherik, Y.O. Elakwah, M.F.A. Goosen, Single asperity nanoscratch behaviour of HIPed and cast Stellite 6 alloys, Wear. 312 (2014) 70–82.

[8] J. V. Giacchi, C.N. Morando, O. Fornaro, H.A. Palacio, Microstructural characterization of as-cast biocompatible Co-Cr-Mo alloys, Mater. Charact. 62 (2011) 53–61.

[9] C.D. Opris, R. Liu, M.X. Yao, X.J. Wu, Development of Stellite alloy composites with sintering/HIPing technique for wear-resistant applications, Mater. Des. 28 (2007) 581–591.

[10] B. Patel, G. Favaro, F. Inam, M.J. Reece, A. Angadji, W. Bon, J. Huang, M. Edirisinghe, Cobalt-based orthopaedic alloys : Relationship between forming route , microstructure and tribological performance, 32 (2012) 1222–1229.

[11] P. Budzynski, M. Kaminski, M. Wiertel, K. Pyszniak, A. Droździel, Mechanical properties of the stellite 6 cobalt alloy implanted with nitrogen ions, Acta Phys. Pol. A. 132 (2017) 203–205.

[12] H.Ö. Gülsoy, Ö. Özgün, S. Bilketay, Powder injection molding of Stellite 6 powder: Sintering, microstructural and mechanical properties, Mater. Sci. Eng. A. 651 (2016) 914–924.

[13] M.X. Yao, J.B.C. Wu, W. Xu, R. Liu, Metallographic study and wear resistance of a high-C wrought Co-based alloy Stellite 706K, Mater. Sci. Eng. A. 407 (2005) 291–298.

[14] P. Mengucci, G. Barucca, A. Gatto, E. Bassoli, L. Denti, F. Fiori, E. Girardin, P. Bastianoni, B. Rutkowski, A. Czyrska-Filemonowicz, Effects of thermal treatments on microstructure and mechanical properties of a Co-Cr-Mo-W biomedical alloy produced by laser sintering, J. Mech. Behav. Biomed. Mater. 60 (2016) 106–117.

[15] B. Ren, C. Chen, M. Zhang, Effect of heat treatment on the microstructure of Co-Cr-W alloy fabricated by laser additive manufacturing, Opt. Eng. 57 (2018) 041409.

[16] X. Yan, H. Lin, Y. Wu, W. Bai, Effect of two heat treatments on mechanical properties of selective-laser-melted Co-Cr metal-ceramic alloys for application in thin removable partial dentures, J. Prosthet. Dent. 119 (2018) 1028.e1-1028.e6.

[17] Y. Kajima, A. Takaichi, N. Kittikundecha, T. Nakamoto, T. Kimura, N. Nomura, A. Kawasaki, T. Hanawa, H. Takahashi, N. Wakabayashi, Effect of heat-treatment

temperature on microstructures and mechanical properties of Co–Cr–Mo alloys fabricated by selective laser melting, Mater. Sci. Eng. A. 726 (2018) 21–31.
[18] Y. Lu, S. Wu, Y. Gan, S. Zhang, S. Guo, J. Lin, J. Lin, Microstructure , mechanical property and metal release of As-SLM CoCrW alloy under different solution treatment conditions, J. Mech. Behav. Biomed. Mater. 55 (2015) 179–190.
[19] K. Myers, P. Cortes, B. Conner, T. Wagner, B. Hetzel, K.M. Peters, Structure property relationship of metal matrix syntactic foams manufactured by a binder jet printing process, Addit. Manuf. 5 (2015) 54–59.
[20] A. Mostafaei, E.L. Stevens, E.T. Hughes, S.D. Biery, C. Hilla, M. Chmielus, Powder bed binder jet printed alloy 625: Densification, microstructure and mechanical properties, Mater. Des. 108 (2016) 126–135.
[21] A. Mostafaei, P. Rodriguez De Vecchis, E.L. Stevens, M. Chmielus, Sintering regimes and resulting microstructure and properties of binder jet 3D printed Ni-Mn-Ga magnetic shape memory alloys, Acta Mater. 154 (2018) 355–364.
[22] A. Mostafaei, K.A. Kimes, E.L. Stevens, J. Toman, Y.L. Krimer, K. Ullakko, M. Chmielus, Microstructural evolution and magnetic properties of binder jet additive manufactured Ni-Mn-Ga magnetic shape memory alloy foam, Acta Mater. 131 (2017) 482–490.
[23] A. Mostafaei, J. Toman, E.L. Stevens, E.T. Hughes, Y.L. Krimer, M. Chmielus, Microstructural evolution and mechanical properties of differently heat-treated binder jet printed samples from gas- and water-atomized alloy 625 powders, Acta Mater. 124 (2017) 280–289.
[24] A. Mostafaei, E.L. Stevens, J.J. Ference, D.E. Schmidt, M. Chmielus, Binder jetting of a complex-shaped metal partial denture framework, Addit. Manuf. 21 (2018) 63–68.
[25] A. Levy, A. Miriyev, A. Elliott, S.S. Babu, N. Frage, Additive manufacturing of complex-shaped graded TiC/steel composites, Mater. Des. (2017).
[26] D.-T. Chou, D. Wells, D. Hong, B. Lee, H. Kuhn, P.N. Kumta, Novel processing of iron–manganese alloy-based biomaterials by inkjet 3-D printing, Acta Biomater. 9 (2013) 8593–8603.
[27] D. Hong, D.T. Chou, O.I. Velikokhatnyi, A. Roy, B. Lee, I. Swink, I. Issaev, H.A. Kuhn, P.N. Kumta, Binder-jetting 3D printing and alloy development of new biodegradable Fe-Mn-Ca/Mg alloys, Acta Biomater. 45 (2016) 375–386.
[28] A. Butscher, M. Bohner, N. Doebelin, L. Galea, O. Loeffel, R. M??ller, Moisture based three-dimensional printing of calcium phosphate structures for scaffold engineering, Acta Biomater. 9 (2013) 5369–5378. doi:10.1016/j.actbio.2012.10.009.
[29] A. Zocca, P. Colombo, C.M. Gomes, J. Günster, Additive Manufacturing of Ceramics: Issues, Potentialities, and Opportunities, J. Am. Ceram. Soc. 98 (2015) 1983–2001.
[30] W.S.W. Harun, M.S.I.N. Kamariah, N. Muhamad, S.A.C. Ghani, F. Ahmad, Z. Mohamed, A review of powder additive manufacturing processes for metallic biomaterials, Powder Technol. 327 (2018) 128–151.
[31] A. Basalah, Y. Shanjani, S. Esmaeili, E. Toyserkani, Characterizations of additive manufactured porous titanium implants, J. Biomed. Mater. Res. - Part B Appl. Biomater. 100 B (2012) 1970–1979.
[32] J.K. Sherwood, S.L. Riley, R. Palazzolo, S.C. Brown, C. Monkhouse, M. Coates, L.G. Griffith, L.K. Landeen, A. Ratcliffe, A three-dimensional osteochondral composite scaffold for articular cartilage repair, Biomaterials. 23 (2002) 4739–4751.

[33] M.N. Islam, S. Sacks, An experimental investigation into the dimensional error of powder-binder three-dimensional printing, Int. J. Adv. Manuf. Technol. 82 (2016) 1371–1380.
[34] A. Mostafaei, C. Hilla, E.L. Stevens, P. Nandwana, A.M. Elliott, M. Chmielus, Comparison of characterization methods for differently atomized nickel-based alloy 625 powders, Powder Technol. 333 (2018) 180–192.
[35] R. Liu, S.Q. Xi, S. Kapoor, X.J. Wu, Investigation of solidification behavior and associate microstructures of Co-Cr-W and Co-Cr-Mo alloy systems using DSC technique, J. Mater. Sci. 45 (2010) 6225–6234.
[36] C.A. Schneider, W.S. Rasband, K.W. Eliceiri, NIH Image to ImageJ: 25 years of image analysis, Nat. Methods. 9 (2012) 671–675.
[37] ASM-Standard, Metallography and Microstructures of Nonferrous Alloys, ASM Handb. 9 (2004) 711–751.
[38] A. Mostafaei, P. Rodriguez De Vecchis, I. Nettleship, M. Chmielus, Effect of powder size distribution on densification and microstructural evolution of binder-jet 3D-printed alloy 625, Mater. Des. 162 (2019) 375–383.
[39] U. Malayoglu, A. Neville, Comparing the performance of HIPed and Cast Stellite 6 alloy in liquid-solid slurries, Wear. 255 (2003) 181–194.
[40] A. Simchi, Densification and microstructural evolution during co-sintering of Ni-base superalloy powders, Metall. Mater. Trans. A Phys. Metall. Mater. Sci. 37 (2006) 2549–2557.
[41] D. Klarstrom, P. Crook, J. Wu, Metallography and microstructures of cobalt and cobalt alloys, G.F. Vander Voort (Ed.), ASM Handbook, Volume 9: Metallography and Microstructures, ASM International, Metals Park, OH, USA, 2004.
[42] K. Nová, P. Novák, D. Dvorský, Influence of alloying elements on the mechanical properties of a cobalt-based alloy produced with powder metallurgy, Mater. Tehnol. 51 (2017) 443–447.
[43] A. Khoddamzadeh, R. Liu, M. Liang, Q. Yang, Wear resistant carbon fiber reinforced Stellite alloy composites, Mater. Des. 56 (2014) 487–494.
[44] M. Mori, K. Yamanaka, A. Chiba, Effect of cold rolling on phase decomposition in biomedical Co-29Cr-6Mo-0.2N alloy during isothermal heat treatment at 1073 K, J. Alloys Compd. 612 (2014) 273–279. doi:10.1016/j.jallcom.2014.05.175.
[45] S. Kurosu, H. Matsumoto, A. Chiba, Isothermal phase transformation in biomedical Co-29Cr-6Mo alloy without addition of carbon or nitrogen, Metall. Mater. Trans. A Phys. Metall. Mater. Sci. 41 (2010) 2613–2625.
[46] S. Zangeneh, M. Ketabchi, H.F. Lopez, Nanoscale carbide precipitation in Co-28Cr-5Mo-0.3C implant alloy during martensite transformation, Mater. Lett. 116 (2014) 188–190.
[47] K. Yamanaka, M. Mori, Y. Torita, A. Chiba, Impact of minor alloying with C and Si on the precipitation behavior and mechanical properties of N-doped Co–Cr alloy dental castings, Mater. Sci. Eng. C. 92 (2018) 112–120.
[48] T. Kilner, Phase identification and incipient melting in a cast Co-Cr surgical implant alloy, 16 (1982) 63–79.
[49] X.P. Tan, P. Wang, Y. Kok, W.Q. Toh, Z. Sun, S.M.L. Nai, M. Descoins, D. Mangelinck, E. Liu, S.B. Tor, Carbide precipitation characteristics in additive manufacturing of Co-Cr-Mo alloy via selective election beam melting, Scr. Mater. 143 (2018) 117–121.
[50] P. Crook, Cobalt and Cobalt Alloys, in: ASM Handbook: Properties and Selection:

Nonferrous Alloys and Special-Purpose Materials, 1990.
[51] G.. Kuczynski, The mechanism of densification during sintering of metallic particles, Acta Metall. 4 (1956) 58–61.
[52] J.G.R. Rockland, The determination of the mechanism of sintering, Acta Metall. 15 (1967) 277–286.
[53] Y. Liao, R. Pourzal, P. Stemmer, M.A. Wimmer, J.J. Jacobs, A. Fischer, L.D. Marks, New insights into hard phases of CoCrMo metal-on-metal hip replacements, J. Mech. Behav. Biomed. Mater. 12 (2012) 39–49.
[54] K. Yamanaka, M. Mori, A. Chiba, Refinement of solidification microstructures by carbon addition in biomedical Co-28Cr-9W-1Si alloys, Mater. Lett. 116 (2014) 82–85.

Table Captions:

Table 1. Chemical composition in [wt.-%] of Stellite 6 powder Reported by the manufacturer.

Co	Cr	W	Ni	Mn	C	Si	Fe	Mo	P	S
Bal.	30.2	4.5	1.9	1.2	1.1	1.0	0.9	0.7	<0.005	<0.005

Table 2. Image analysis results on OM micrographs (shown in Figure 3) obtained from the BJ3DP Stellite 6 samples sintered between 1260 °C and 1310 °C. Sintering at 1300 °C led to the maximum relative density thus aging treatment was carried out to characterize microstructural evolution as well as properties of the heat-treated BJ3DP Stellite 6 part. Dark grey areas are precipitates defined as within grain Cr-rich carbides and eutectic carbides at the grain boundaries. Complementary elemental analysis will be discussed shortly.

Samples	Solid volume fraction [%]	Porosity [%]	Cr-rich fraction as carbides [%]		Co-rich fraction as matrix [%]	Grain size [µm]	Pore size [µm]
			Within grain	At grain boundaries (eutectic carbides)			
Sintered at 1260 °C	56.3 ± 1.7	43.7 ± 1.9	11.4 ± 1.5	n/a[1]	44.8 ± 1.9	63.6 ± 2.3	--- [2]
Sintered at 1270 °C	58.1 ± 0.9	41.9 ± 0.8	13.9 ± 4.3	n/a	44.2 ± 1.1	69.7 ± 6.3	---
Sintered at 1280 °C	70.7 ± 1.1	29.3 ± 0.9	10.1 ± 3.8	5.6 ±1.2	55.0 ± 0.8	88.5 ± 7.4	---
Sintered at 1290 °C	97.4 ± 0.8	2.6 ± 0.5	n/a	15.7 ± 2.4	83.7 ± 2.5	99.7 ± 9.8	8.2 ± 4.3
Sintered at 1300 °C	99.8 ± 0.2	~0.2	n/a	16.8 ± 0.1	83.1 ± 0.1	97.8 ± 6.2	6.2 ± 0.9
Sintered at 1310 °C	99.8 ± 0.3	~0.2	n/a	21.4 ±1.7	78.4 ± 1.7	94.3 ± 4.9	4.8 ± 2.1
Sintered at 1300 °C and aged at 900 °C for 10 h	99.9 ± 0.1	~0.1	< 1% *	27.7 ± 2.2	71.8 ± 2.4	93.5 ± 2.9	3.1 ± 1.2

[1] n/a: It means that no precipitate was seen in the optical or electron micrographs within grain/at boundaries.

[2] ---: Continuous network of porosity is present.

* Few precipitates enriched in Cr-Mn-C were seen in the SEM observations (see Figure 7).

Table 3. Measured carbon, oxygen and nitrogen content of the as-received Stellite 6 powder, binder jetted cured samples and post heat treated parts in [wt.-%].

Samples	Carbon	Oxygen	Nitrogen
	[wt.-%]		
As-received Stellite 6 powder	1.238	0.058	0.025
Binder jetted and cured parts	1.570	0.114	0.142
Sintered at 1260 °C	0.800	0.030	0.059
Sintered at 1280 °C	0.792	0.055	0.067
Sintered at 1300 °C	0.803	0.003	0.007
Sintered at 1300 °C and aged at 900 °C for 10 h	0.892	0.004	0.003

Figure Captions:

Figure 1. (a) Particle size distribution result and (b) SEM micrographs of the Stellite 6 powder.

Figure 2. Comparison between variations in the relative bulk and average densities (obtained from Archimedes method) with the solid volume fraction results (obtained from optical micrograph analysis using ImageJ software) for the differently sintered BJ3DP parts from Stellite 6.

Figure 3. Optical micrographs of polished samples after sintering at different temperatures (a) 1260 °C, (b) 1270 °C, (c) 1280 °C, (d) 1290 °C, (e) 1300 °C and (f) 1310 °C with a holding time of 1 h (magnification 200× and 500×). It was seen that the pore distribution changes with increasing sintering temperature resulting in higher density of the BJ3DP part. Above 1290 °C, eutectic carbides formed at the grain boundaries.

Figure 4. Scanning electron micrographs with EDS mapping elemental analysis results taken from the BJ3DP samples sintered at (a) 1260 °C, (b) 1280 °C and (c) 1300 °C.

Figure 5. Optical micrographs of polished samples after (a,b) sintering at 1300 °C for 1 h and (c,d) additional aging at 900 °C for 10 h (magnification 200× and 500×). After aging, the fraction of eutectic carbides at grain boundaries grew while the grains consisting of Co-rich matrix shrunk. Quantitative analysis results are given in Table 2.

Figure 6. SEM micrographs of polished samples after (a,b) sintering at 1300 °C for 1 h and (c,d) aging at 900 °C for 10 h (region of higher magnification are indicated by dashed box). After aging, eutectic carbides grew at the boundaries while the grains size of Co-rich grains decreased. Intragranular striations in c and d indicate a martensitic phase transformation after aging from fcc to hcp.

Figure 7. Scanning electron micrograph with EDS mapping elemental analysis results taken from the BJ3DP sample sintered at 1300 °C for 1 h followed by aging (900 °C for 10 h).

Figure 8. XRD patterns taken from as-received Stellite 6 powder, and after BJ3DP followed by sintering at different temperatures (and aging).

Figure 9. (a) Hardness values and (b) stress-strain curves obtained from the BJ3DP Stellite 6 samples depending on the sintering temperature and aging treatment. SEM micrographs insets were taken from the fracture surface of a sintered sample (1300 °C, 1 h) and additionally aged sample (900 °C, 10 h).

Figure 10. (A) Schematic showing phase formation and microstructure evolution model for differently heat-treated BJ3DP Stellite 6. (B) Detailed microstructural model with relevant information about phase formation during sintering and aging treatment.

Figure 11. Thermodynamic modeling results of (a) equilibrium-phase fractions of Co–30Cr–4.5W–Si-0.8C system as a function of temperature predicted by the Scheil-Gulliver model and (b) equilibrium step diagram predicted using TCFE6-TCS Steels/Fe-Alloys Database in Thermo-calc® software.

Figure 12. Photographs of prototype sample parts binder jet 3D printed from Stellite 6. Top row displays green parts and bottom row indicates sintered samples at 1280 °C for 1 h. (a,e) top-view and (b,f) bottom-view taken from a partial denture; and (c,g) back-view and (d,h) front-view taken from a knee joint.

Figure 13. In vitro cytotoxicity of NIH/3T3 fibroblasts cultured on Stellite 6 discs. (A) Fluorescent Live-Dead images of cells after 48-h culture. *Left to right: Stellite 6, cell culture treated polystyrene (+Control), cell culture treated polystyrene – ethanol-killed cells (-Control).* (B) Cell viability displayed as a percentage of live cells. (C) Number of Live/Dead cells per 4X magnification field for each treatment group. Statistical significance was observed between treatment groups denoted by different letters, analyzed by factor: Cell Viability (a-b); Live (a-c)/Dead (e-f) cells. (a-f = $p < 0.0001$, error bars are represented as SEM).

Figure 1

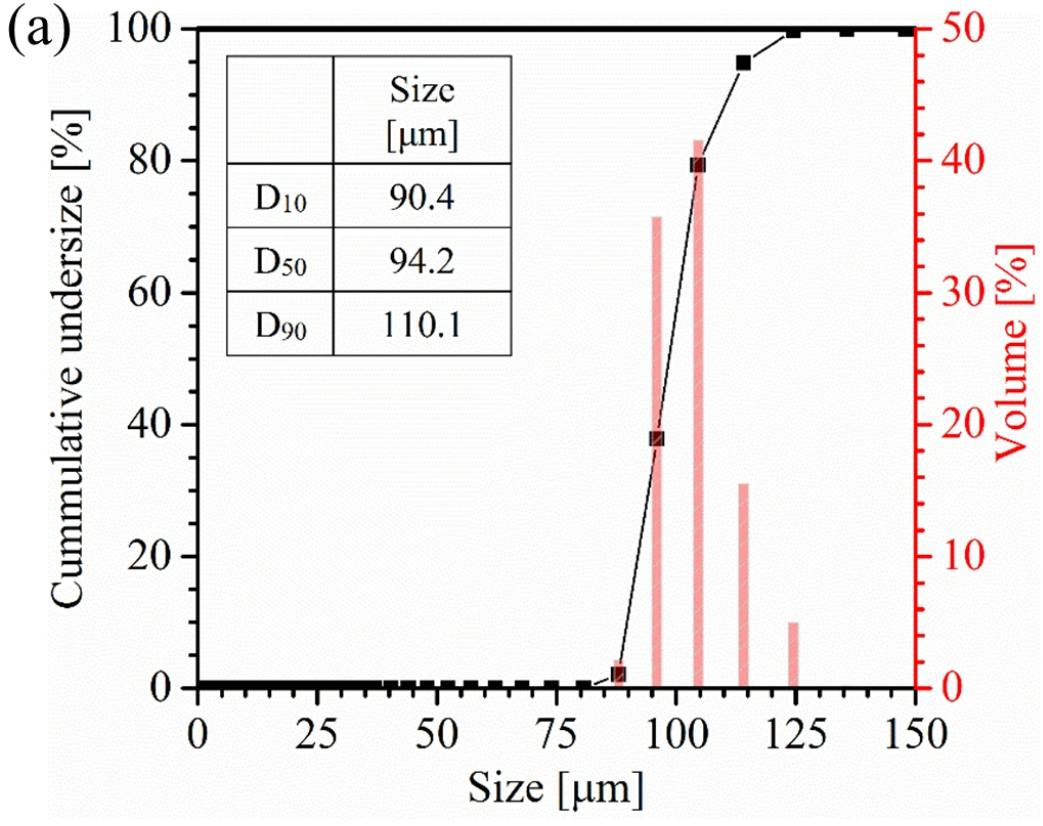
(a)
Size [µm]
D10 90.4
D50 94.2
D90 110.1
Cummulative undersize [%]
Volume [%]
Size [µm]
0
20
40
60
80
100
0
10
20
30
40
50
0
25
50
75
100
125
150

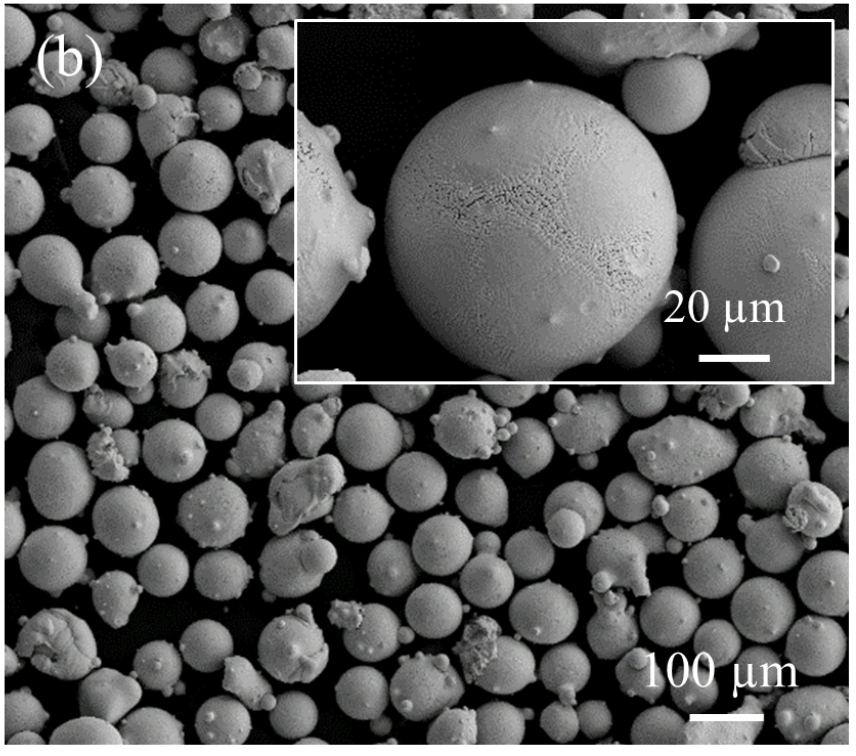
(b)
20 µm
100 µm

Figure 2

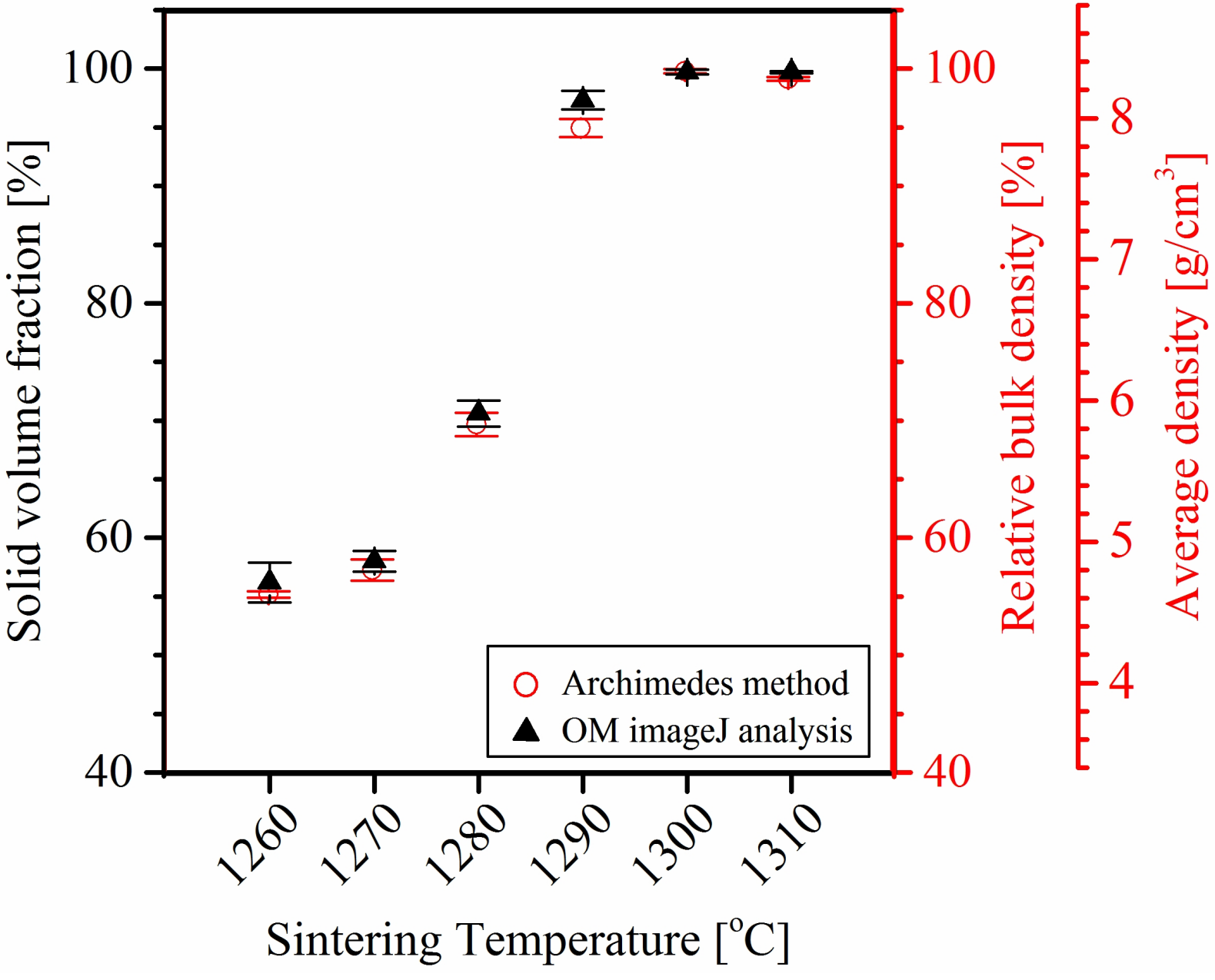
Solid volume fraction [%]
100
80
60
40
Relative bulk density [%]
100
80
60
40
Average density [g/cm^3]
8
7
6
5
4
1260
1270
1280
1290
1300
1310
Sintering Temperature [°C]
Archimedes method
OM imageJ analysis

Figure 3

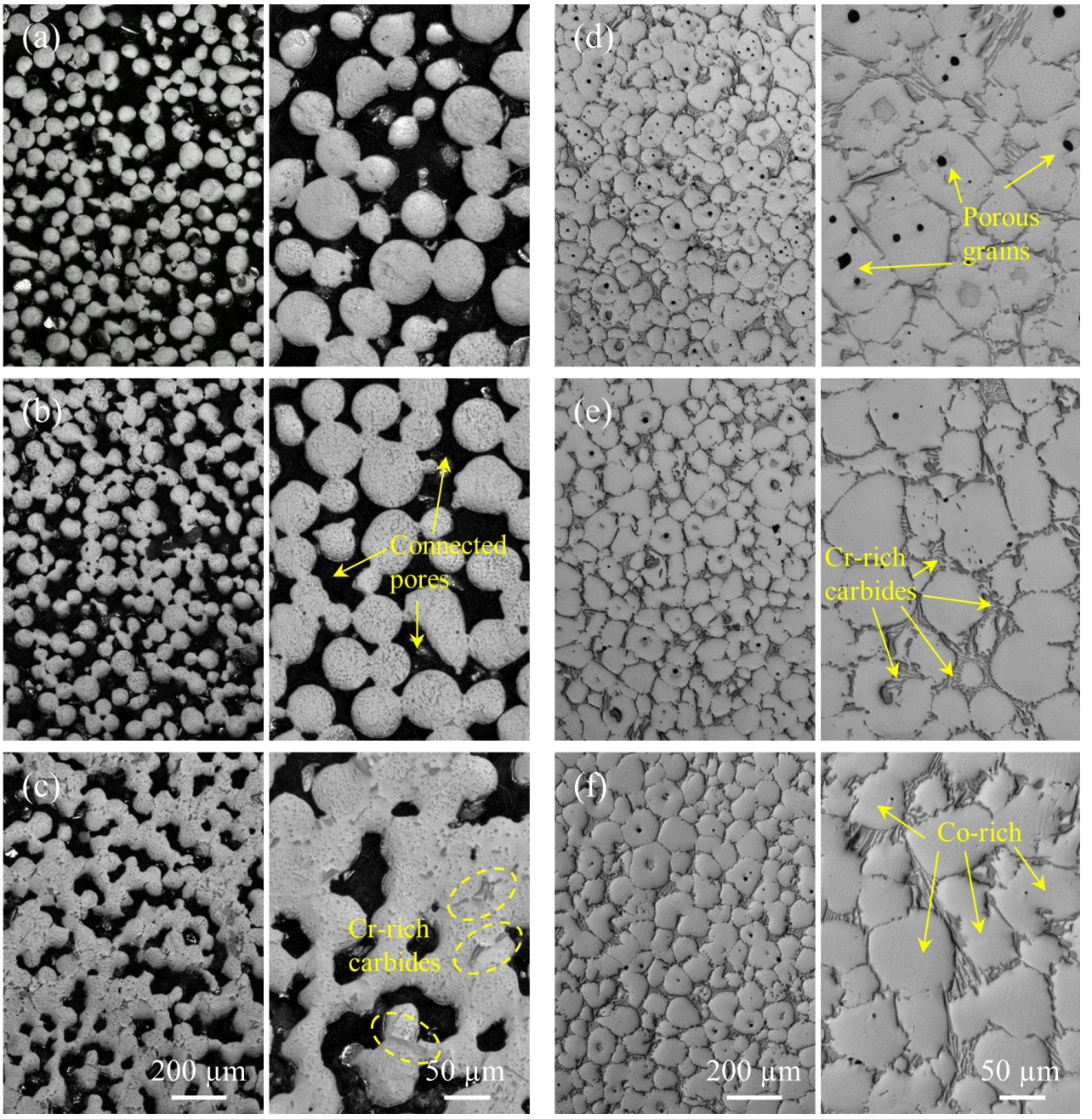
(a)
(b)
Connected pores
(c)
Cr-rich carbides
200 μm
50 μm
(d)
Porous grains
(e)
Cr-rich carbides
(f)
Co-rich
200 μm
50 μm

Figure 4

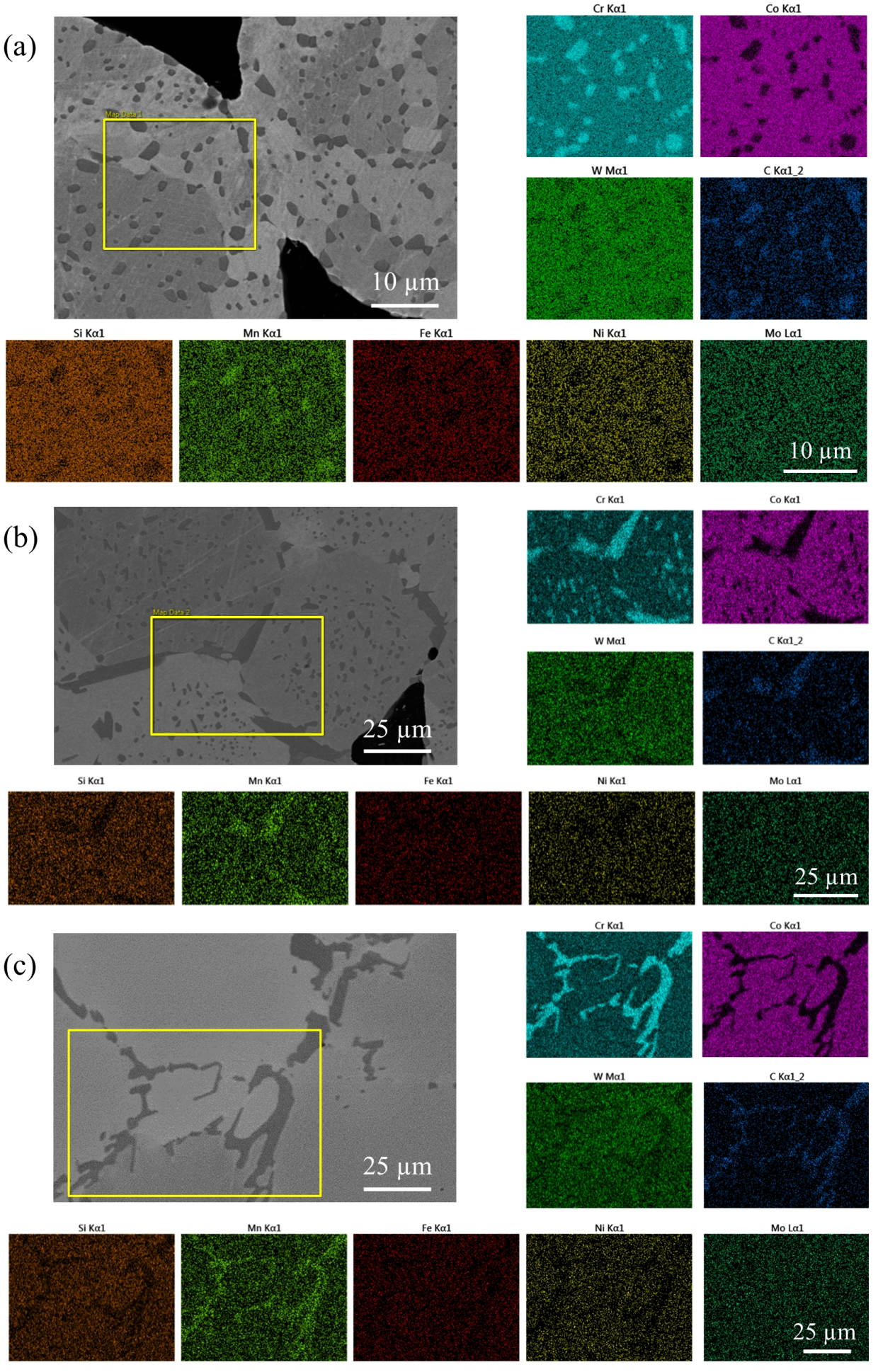
(a)
Map Data 1
10 μm
Cr Kα1
Co Kα1
W Mα1
C Kα1_2
Si Kα1
Mn Kα1
Fe Kα1
Ni Kα1
Mo Lα1
10 μm
(b)
Map Data 2
25 μm
Cr Kα1
Co Kα1
W Mα1
C Kα1_2
Si Kα1
Mn Kα1
Fe Kα1
Ni Kα1
Mo Lα1
25 μm
(c)
25 μm
Cr Kα1
Co Kα1
W Mα1
C Kα1_2
Si Kα1
Mn Kα1
Fe Kα1
Ni Kα1
Mo Lα1
25 μm

Figure 5

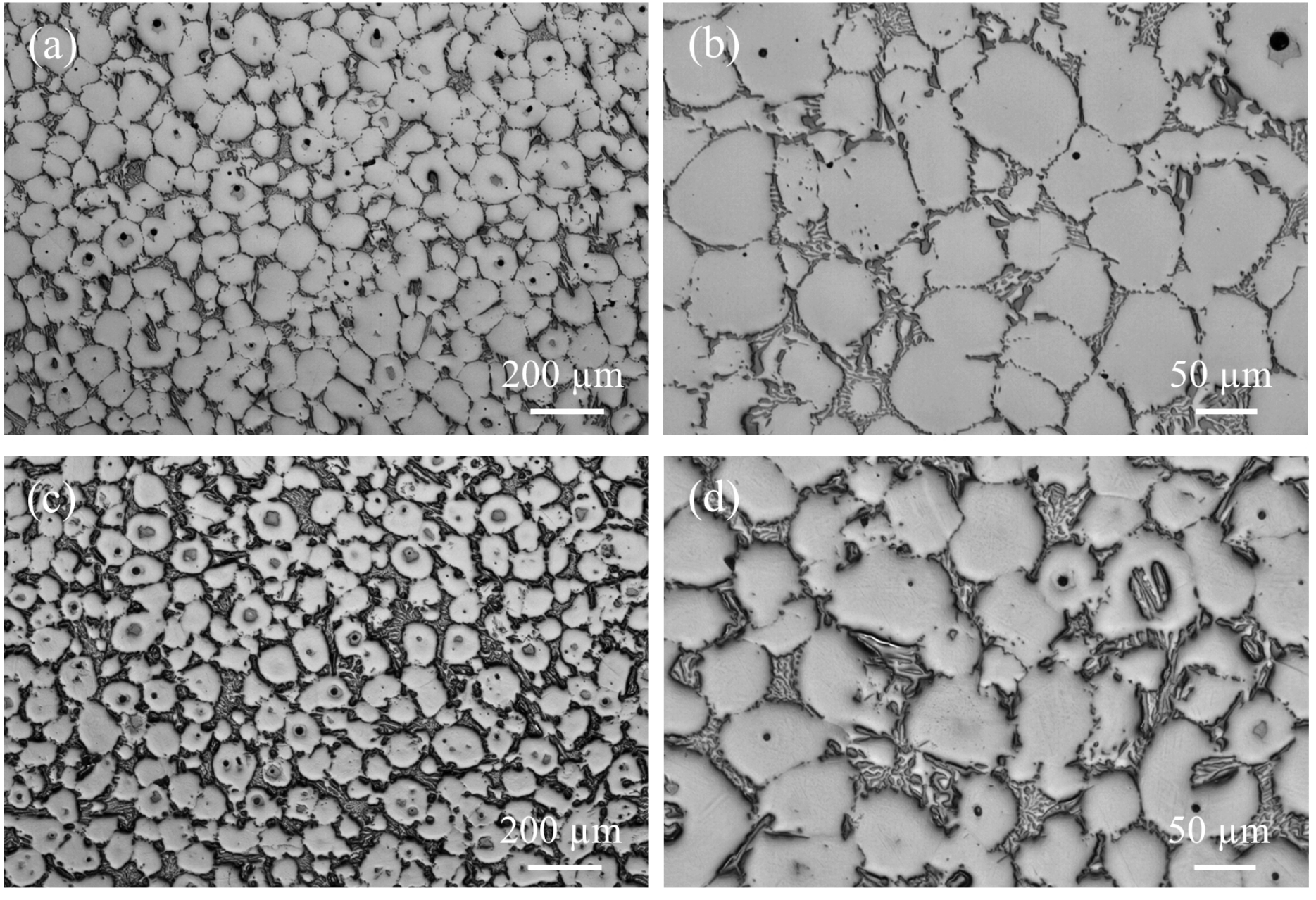

Figure 6

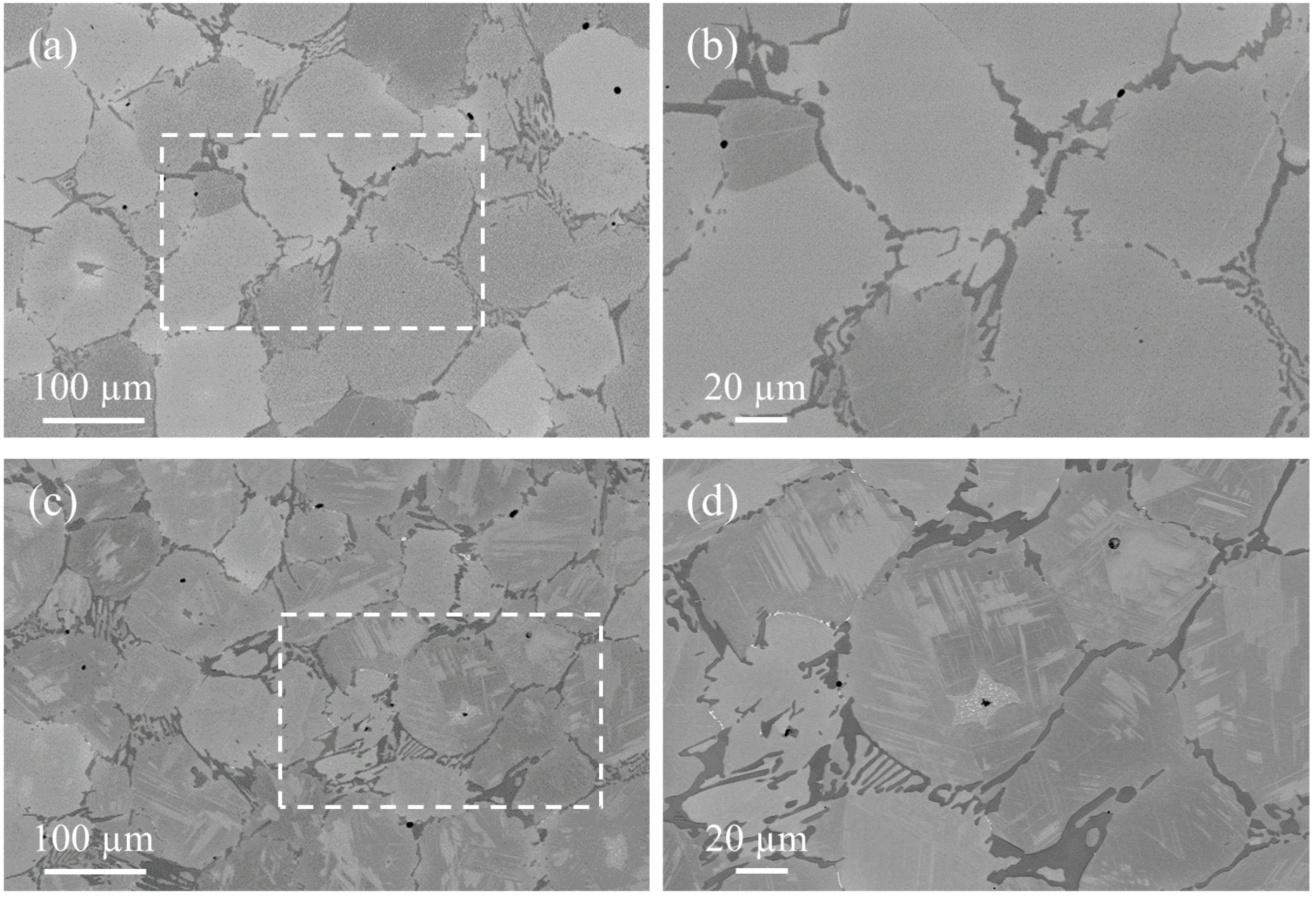

Figure 7

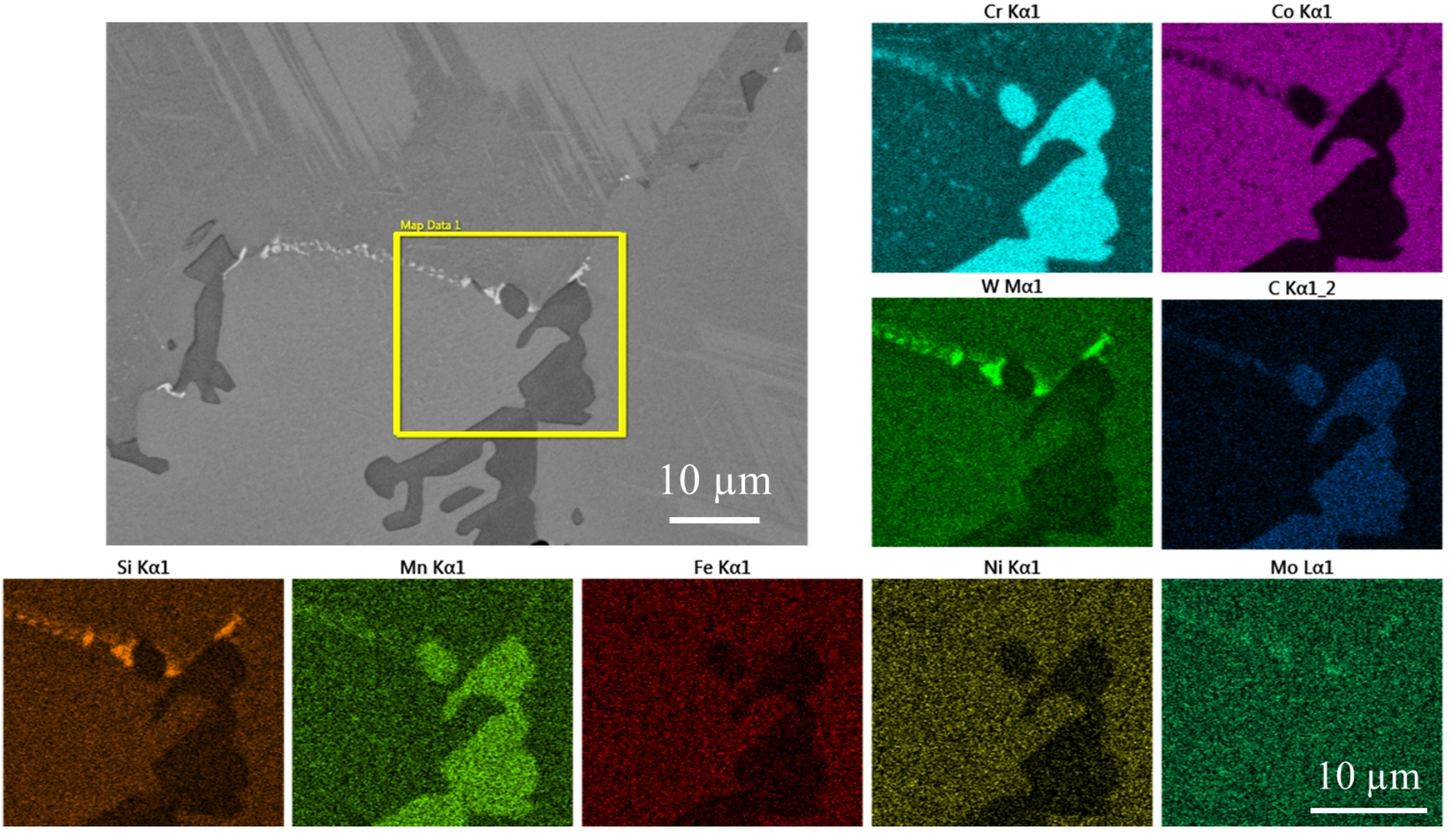
Map Data 1
10 µm
Cr Kα1
Co Kα1
W Mα1
C Kα1_2
Si Kα1
Mn Kα1
Fe Kα1
Ni Kα1
Mo Lα1
10 µm

Figure 8

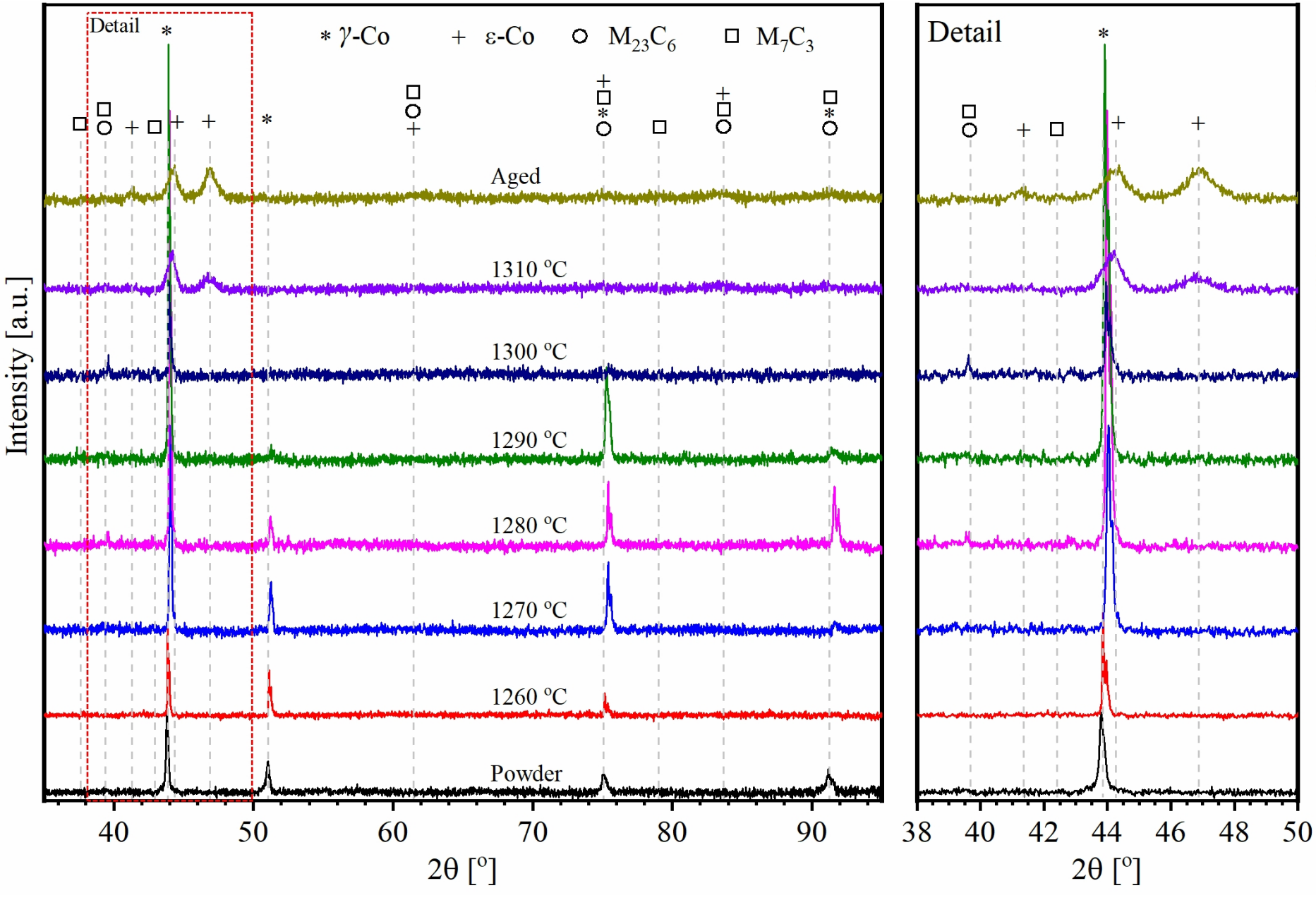
Detail
* γ-Co
+ ε-Co
○ M23C6
□ M7C3
Aged
1310 °C
1300 °C
1290 °C
1280 °C
1270 °C
1260 °C
Powder
Intensity [a.u.]
40
50
60
70
80
90
2θ [°]
Detail
38
40
42
44
46
48
50
2θ [°]

Figure 9

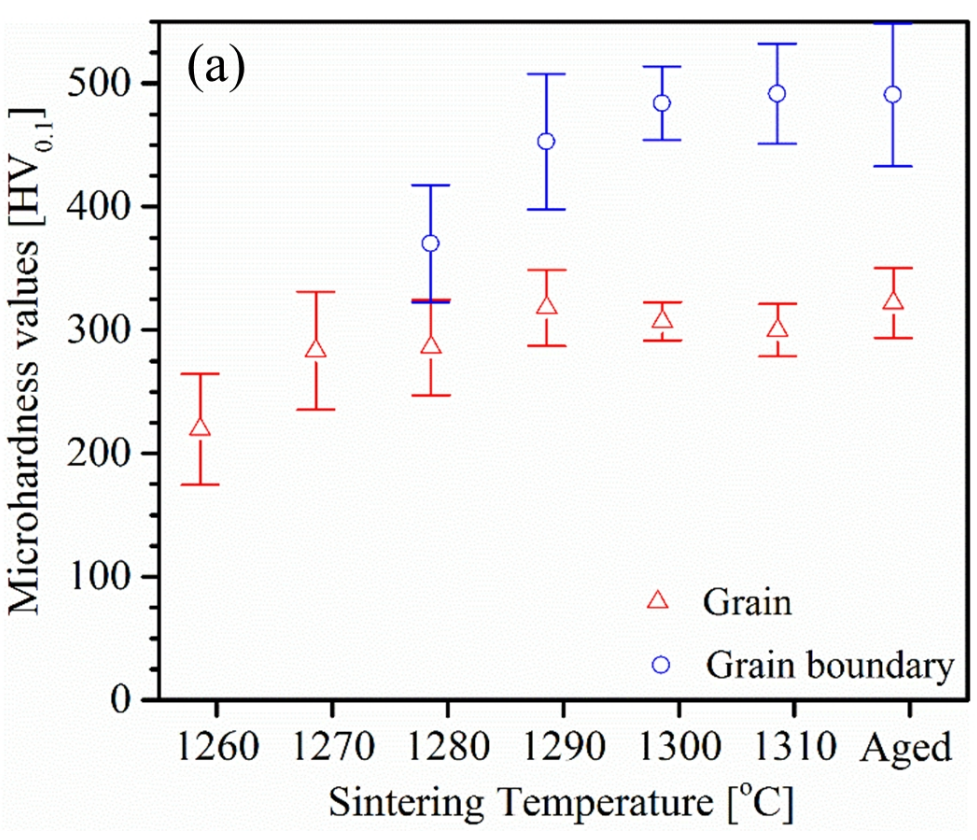
(a)
Microhardness values [HV0.1]
0
100
200
300
400
500
Grain
Grain boundary
1260
1270
1280
1290
1300
1310
Aged
Sintering Temperature [°C]

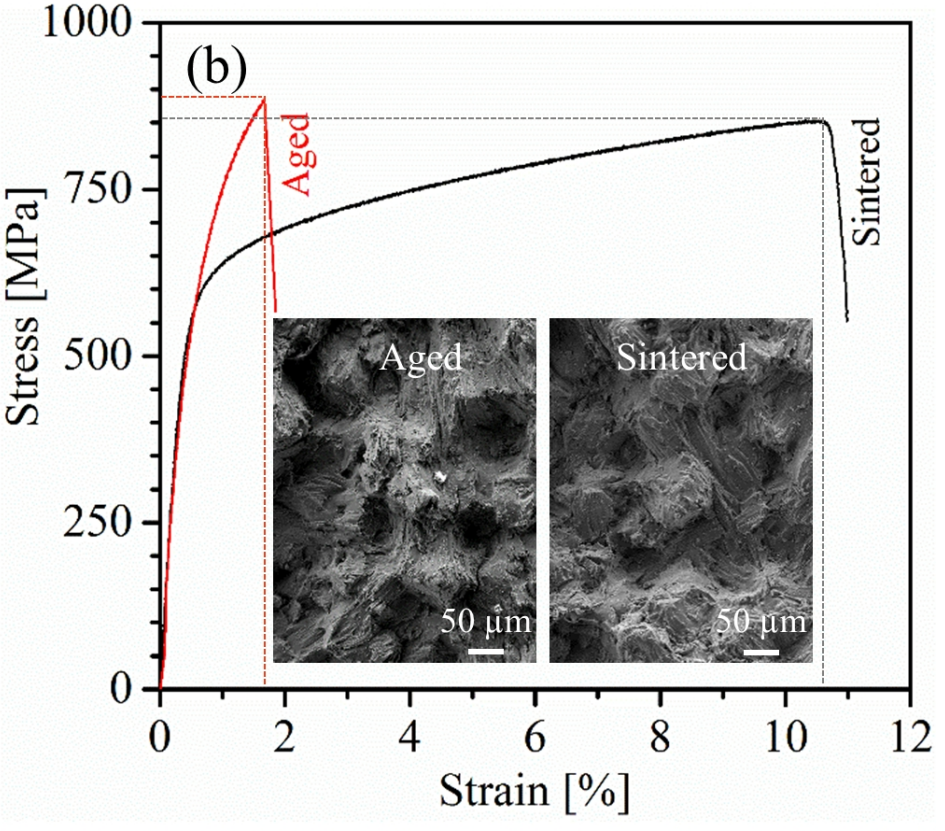
(b)
Stress [MPa]
0
250
500
750
1000
Aged
Sintered
Aged
50 µm
Sintered
50 µm
0
2
4
6
8
10
12
Strain [%]

Figure 10

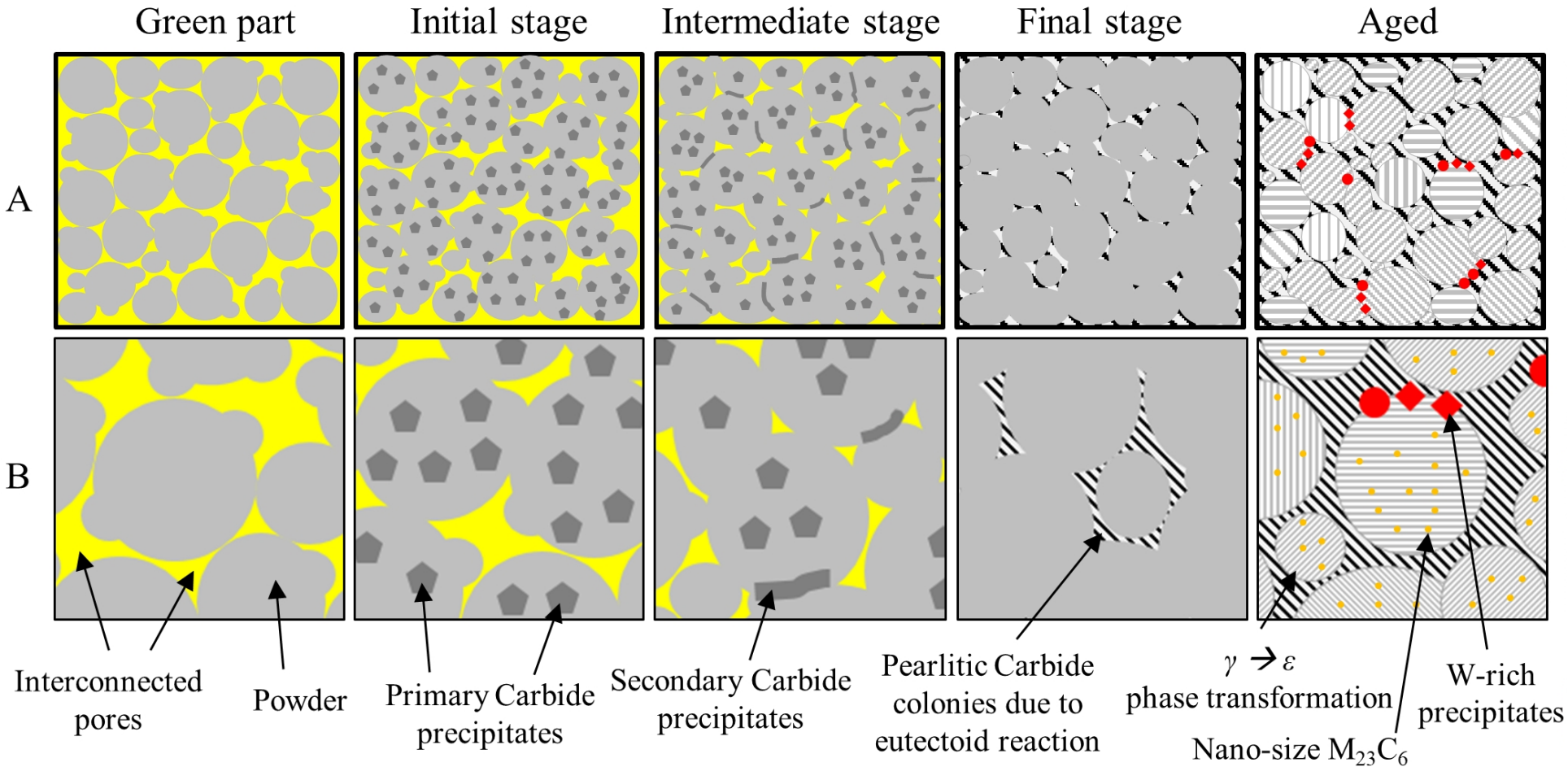
Green part
Initial stage
Intermediate stage
Final stage
Aged
A
B
Interconnected pores
Powder
Primary Carbide precipitates
Secondary Carbide precipitates
Pearlitic Carbide colonies due to eutectoid reaction
γ → ε phase transformation
Nano-size M23C6
W-rich precipitates

Figure 11

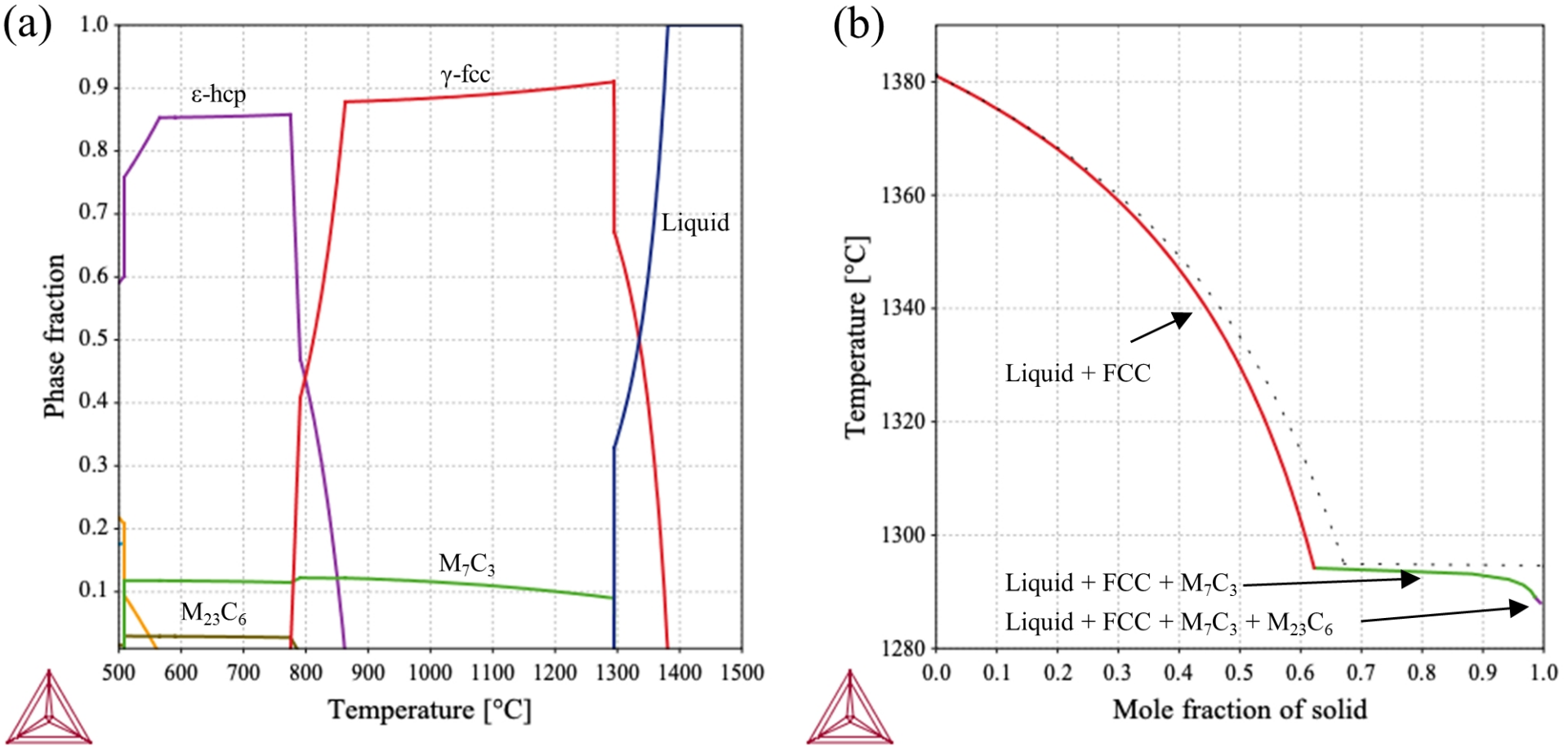
(a)
Phase fraction
Temperature [°C]
ε-hcp
γ-fcc
Liquid
M7C3
M23C6
(b)
Temperature [°C]
Mole fraction of solid
Liquid + FCC
Liquid + FCC + M7C3
Liquid + FCC + M7C3 + M23C6

Figure 12

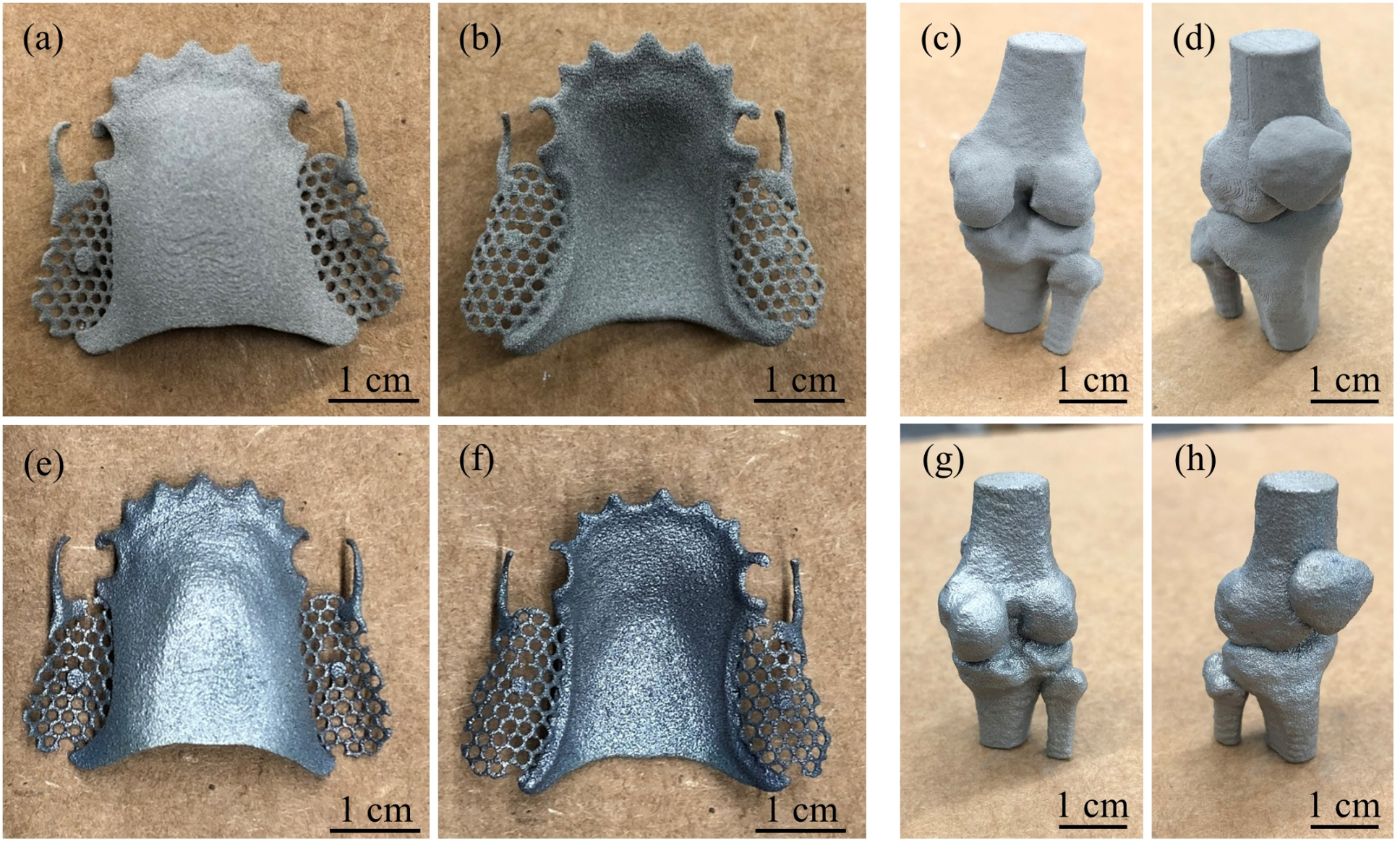

Figure 13

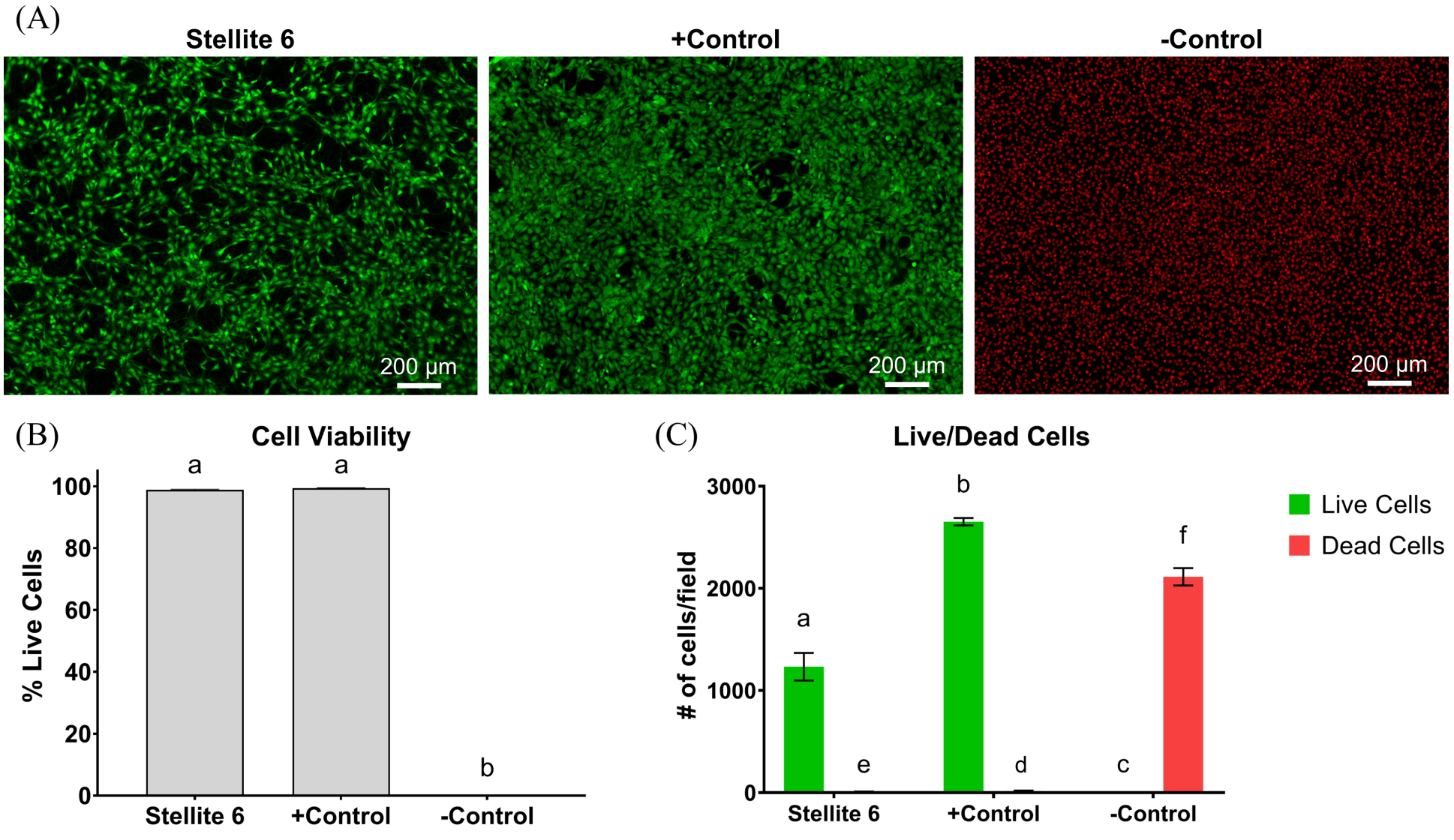
(A)
Stellite 6
+Control
-Control
200 µm
200 µm
200 µm
(B)
Cell Viability
% Live Cells
100
80
60
40
20
0
a
a
b
Stellite 6
+Control
-Control
(C)
Live/Dead Cells
# of cells/field
3000
2000
1000
0
a
e
b
d
c
f
Stellite 6
+Control
-Control
Live Cells
Dead Cells